SANDIA REPORT
SAND2006-6931
Unlimited Release
Printed November 2006

Bioagent Detection Using Miniaturized NMR and Nanoparticle Amplification: Final LDRD Report

Todd M. Alam, Catherine F. M. Clewett, David P. Adams, John D. Williams, Hongyou Fan, Andrew F. McDowell, Natalie L. Aldolphi, and Laurel O. Sillerud

Prepared by
Sandia National Laboratories
Albuquerque, New Mexico 87185 and Livermore, California 94550

Sandia is a multiprogram laboratory operated by Sandia Corporation,
a Lockheed Martin Company, for the United States Department of Energy's
National Nuclear Security Administration under Contract DE-AC04-94AL85000.

Issued by Sandia National Laboratories, operated for the United States Department of Energy by Sandia Corporation.

Available to DOE and DOE contractors from
U.S. Department of Energy
Office of Scientific and Technical Information
P.O. Box 62
Oak Ridge, TN 37831

Telephone: (865) 576-8401
Facsimile: (865) 576-5728
E-Mail: reports@adonis.osti.gov
Online ordering: http://www.osti.gov/bridge

Available to the public from
U.S. Department of Commerce
National Technical Information Service
5285 Port Royal Rd.
Springfield, VA 22161

Telephone: (800) 553-6847
Facsimile: (703) 605-6900
E-Mail: orders@ntis.fedworld.gov
Online order: http://www.ntis.gov/help/ordermethods.asp?loc=7-4-0#online

SAND2006-6931
Unlimited Release
Printed November 2006

Bioagent Detection Using Miniaturized NMR and Nanoparticle Amplification: Final LDRD Report

Todd M. Alam [*a], Catherine F. M. Clewett [a], David P. Adams [b], John D. Williams [c], Hongyou Fan [d], Andrew F. McDowell [e], Natalie L. Aldolphi [e] and Laurel O. Sillerud [f]

[a] Department of Electronic and Nanostructured Materials,
[b] Department of Thin Film, Vacuum and Packaging,
[c] Department of Photonics and Microsystems Technology,
[d] Department of Ceramic Processing and Inorganic Materials,
Sandia National Laboratories, Albuquerque, NM

[e] New Mexico Resonance, Albuquerque, NM

[f] Department of Biochemistry and Molecular Biology,
University of New Mexico, Albuquerque, NM

Abstract

This LDRD program was directed towards the development of a portable micro-nuclear magnetic resonance (μ-NMR) spectrometer for the detection of bioagents via induced amplification of solvent relaxation based on superparamagnetic nanoparticles. The first component of this research was the fabrication and testing of two different micro-coil (μ-coil) platforms: namely a planar spiral NMR μ-coil and a cylindrical solenoid NMR μ-coil. These fabrication techniques are described along with the testing of the NMR performance for the individual coils. The NMR relaxivity for a series of water soluble FeMn oxide nanoparticles was also determined to explore the influence of the nanoparticle size on the observed NMR relaxation properties. In addition, The use of commercially produced superparamagnetic iron oxide nanoparticles (SPIONs) for amplification via NMR based relaxation mechanisms was also demonstrated, with the lower detection limit in number of SPIONs per nanoliter (nL) being determined.

* Author to whom correspondence should be addressed: tmalam@sandia.gov

Acknowledgements

The progress made in this LDRD project is the result of contributions from a number of team members both here at Sandia National Laboratories, at the University of New Mexico and the company New Mexico Resonance. These members include C. Clewett, D. P. Adams, C. Benally, A. Fresquez, V. C. Hodges, K. Peterson, M. J. Visale, R. Torres, J. D. Williams, L. O. Sillerud, R. E. Serda, A. F. McDowell, and N. L. Adolphi.

Sandia is multiprogram laboratory operated by Sandia Corporation, a Lockheed Martin Company, for the United Stated Department of Energy's National Nuclear Security Administration under Contract DE-AC04-94AL85000. This work was supported under the Sandia LDRD program (Project 90506).

Definitions

NMR – Nuclear Magnetic Resonance
μ-NMR – Micro-NMR
MRI – Magnetic Resonance Imaging
μ-coil – Micro-coil
SPION – Super Paramagnetic Iron Oxide Nanoparticles
CTAB - Cetyltrimethylammonium Bromide

Table of Contents

List of Figures

List of Tables

Bioagent Detection Using Miniaturized NMR and Nanoparticle Amplification: Final LDRD Report

Executive Summary

The development and testing of two different μ-coil platforms for nuclear magnetic resonance (NMR) detection were completed under this LDRD project. The performance of these NMR μ-coils allowed the demonstration of SPION (superparamagnetic iron oxide nanoparticle) amplification via induced changes in the NMR relaxation rates of the carrier solvent water. A detection limit of 10 particles/nL was experimentally measured for the first prototype solenoid μ-coil design. These results clearly show that nanoparticle amplification for μ-NMR can be used for detection of bioagents.

1. Introduction

The reliable detection of bioagents in a range of sensing environments requires the development of multiple detection platforms. NMR spectroscopy is widely used for the real-time identification of chemical species in solids, liquids and gases because it can easily detect and characterize all components of mixtures without requiring separations or any specific sample preparation. Unfortunately, the low sensitivity of NMR spectroscopy means that the detection limits of biological and chemical warfare agents are many orders below the lethal dose. In addition, high resolution NMR spectroscopy detection of dilute biological agents such as tumor cells, bacteria, bacteria toxins or viruses in fluid samples is complicated by the presence of the dominant background water signal.

However, recent developments in Micro-Electromechanical Systems (MEMS), micro-fluidics and biological nanotechnology have supplied the basis for new applications of NMR with high specificity for the detection and quantification of biological materials in water. The first advance has been the development of superparamagnetic iron oxide nanoparticles (SPIONs) for magnetic resonance imaging (MRI) [1], where they are enjoying multiple applications as biological MRI contrast agents [2-5]. These iron oxide particle systems are also known as SPIO (superparamagnetic iron oxide), WSIO (water-soluble iron oxide), MPIOs (micrometer-size iron oxide particles) and USPIOs (ultra-small dextran-coated iron oxide particles). Nanoparticles can be coupled with biologically specific recognition ligands to target epitopes involved in diseases, like cancer, and has been the focus of fluorescence- based detection schemes [6]. This bio-conjugation can also be detected by NMR using SPIONs and the resulting changes in NMR relaxation properties of the solution. For example, the HER-2 protein is over-produced in many breast cancers and has been the subject of successful NMR imaging experiments where cells displaying this protein have been specifically imaged by means of SPIONs labeled with anti-her-2 antibodies [7-10]. This bio-specific recognition of SPIONs has also been extended to DNA-based nanoparticle assembly [11], and modified phospholipid constructs [12].

The image contrast effects due to SPIONs, which are typically embedded in larger beads, rely on the enhancement of the relaxation rates of water molecules surrounding the beads [13, 14]. The magnetic field gradient from a single, micron-sized magnetic bead has been shown to influence the spin-spin relaxation time (T_2) of the surrounding water within a voxel with dimensions ~100 μm on a side [5] (a volume of ~1 nL), which is

~1000 times larger than that of a single cell. Thus, for a small biological object bound to a magnetic bead in water, the change in the NMR signal caused by the presence of the object is greatly amplified by the effect of the magnetic bead on the surrounding water. In this LDRD project the induced T_2 relaxation effect of the magnetic beads is used not for image contrast, but simply as a means of detecting the presence of these bio-conjugated SPIONs in a small *in-vitro* sample. The generalized principal behind this nano-amplified NMR detection scheme is shown in **Figure 1.**

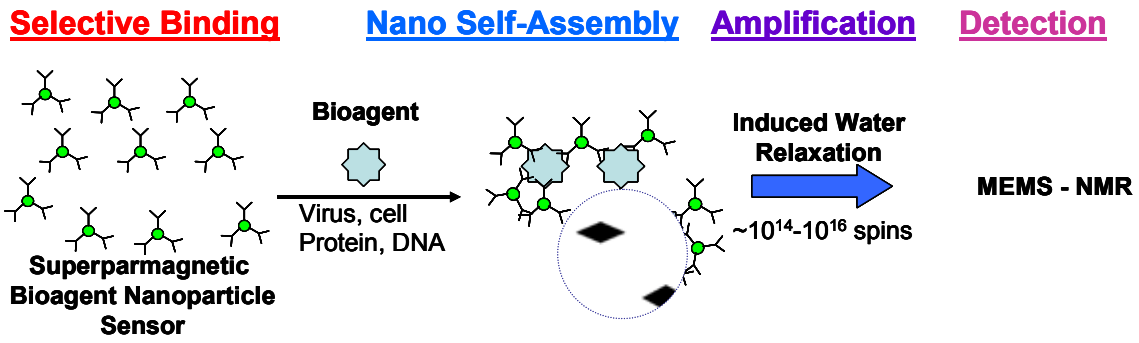

Figure 1: Schematic representation of the nanoparticle amplification.

In principle, a single biological object bound to a magnetic bead can be detected in vitro using a NMR μ-coil with a diameter in the 100 μm range, for which the NMR sample volume is similar to that of the volume influenced by a single bead. This is the motivation for the second component of this research, and it utilizes the development of μ-coils for NMR detection. In recent years significant advances in the development and fabrication of μ-coils (size < 1 mm) for NMR have continued [15-17]. Both planar surface μ-coils and solenoid μ-coils have been developed for a wide range of applications [18-36]. To enhance sensitivity for tiny samples, much of the work with micro-coils has utilized the high fields produced by strong super-conducting magnets, only a limited few

have been directed towards optimization at low magnetic field strengths [37]. However, the small size of a NMR μ-coil suggests a different possibility: the miniaturization of the magnet, and indeed the entire experiment, through the use of small permanent magnets. While the weaker field of a permanent magnet poses a sensitivity challenge, distortions of the magnetic field due to the proximity of the coil to the sample will be reduced at lower fields. Further more, iron oxide particles typically achieve their saturation magnetization in a field of only 0.5–1 Tesla. Thus, for our proposed detection scheme, low-field operation is ideal because it lengthens the T_2 of the background fluid without reducing the T_2 relaxivity of the magnetic beads. Combining μ-coil technology with a compact permanent magnet has the added benefits of reducing the cost, maintenance, and space requirements of the NMR system, and enabling portability. The long-range goal of the research performed under this LDRD is the development of such a portable NMR system capable of detecting minute (even single-particle) quantities of biological materials in fluid samples.

In Section 3 we will describe the synthesis of paramagnetic nanoparticles, and the impact of nanoparticle size on the NMR relaxation properties. In Section 4 we report the development of the solenoid μ-coil for NMR detection, while in Section 5 we describe the development of the planar spiral μ-coil for NMR. In section 6 we demonstrate the amplification of NMR relaxation and detection via SPIONs, while in Section 7 we describe the initial construction of a μ-NMR system here at Sandia National Laboratories.

2. NMR Relaxation by Paramagnetic Nanoparticles

Since the mid 1980's superparamagnetic contrast agents have been pursued for use in MRI. These materials have been based primarily on the water insoluble iron oxide crystal forms of maghemite (γ-Fe_2O_3) or magnetite (Fe_3O_4). A variety of organic modifications have been used to increase the solubility of these iron oxide crystal forms. As an example in Section 3 we describe a series of nanoparticles utilizing either lipid or CTAB (cetyltrimethylammonium bromide) modified surface that greatly increase the water solubility of the iron oxide particles. Nanocrystals of Fe_3O_4 between 4 and 15 nm contain thousands of paramagnetic Fe ions (Fe^{2+} and Fe^{3+}) that are magnetically ordered within the crystal such that the net magnetic moment of the particles are much larger than the individual paramagnetic ion.

Superparamagnetism is characterized by the large magnetic moment of these nanoparticles in the presence of an external magnetic field, while retaining no residual magnetic moment following removal of the external magnetic field. This is in contrast to ferromagnetic particles which retain a magnetic moment at zero magnetic field strength once they have been magnetized. All iron oxide based contrast agents to date are superparamagnetic.

The presence of a large magnetic moment in the superparamagnetic particles changes the NMR relaxation mechanism from the inner-sphere/outer-sphere dipolar relaxation (observed for Gadolinium chelates) to a long-range susceptibility induced relaxation mechanism. The spins experience local field gradients that lead to loss of spin coherence during the NMR experiment.

The susceptibility (χ) is the constant defining the relationship between induced magnetization (M) and the applied magnetic field (H):

$$M = \chi \bullet H \tag{2.1}$$

For iron oxide particles at low magnetic field strengths M is given by:

$$M = Nm^2 \mu_0 H / 3kT \tag{2.2}$$

here N is the number of paramagnetic particles per volume voxel, m is the magnetic moment of paramagnetic particle, μ_0 the free space permeability, k is the Boltzmann's constant and T is the temperature. This allows the susceptibility to be defined by

$$\chi = Nm^2 \mu_0 / 3kT \tag{2.3}$$

This shows that the change in the local susceptibility is proportional to the number of iron oxide particles present and the square of magnetic moment. For superparamagnetic nanoparticles this magnetic moment is commonly the saturation magnetization which is reached for magnetic field strengths between 0.5 to 1.5 Tesla. This saturation magnetization depends on both the size and the aggregation state of the nanoparticles, and will be explored in Section 3.

2.1 NMR Relaxivity

The effectiveness of the relaxation agent on either the spin-spin relaxation rate R_2 (inverse of the relaxation time, = $1/T_2$) or the spin-lattice relaxation rate R_1 (= $1/T_1$) is defined by

$$\begin{aligned} R_2 &= R_2^0 + r_2 C \\ R_1 &= R_1^0 + r_1 C \end{aligned} \tag{2.4}$$

where C is the concentration of the relaxation agent, $R_{2,1}$ are the measured relaxation rates, $R_{2,1}^0$ is the relaxation rate in the absence of agent, and $r_{2,1}$ are the *relaxivity* (units = s^{-1} mM^{-1}). This relaxivity is a measure of how much the relaxation varies with added agent, and is the standard by which different superparamagnetic nanoparticles can be compared.

3. Water Soluble Paramagnetic Nanoparticles

To explore this size and aggregation effect on the NMR relaxation properties noted above a series of FeO and FeMnO nanoparticles were tested. These nanoparticles had well defined and controlled diameters, with different core compositions and surface modifications.

3.1 Synthesis of Fe and FeMnO Oxide Water Soluble Nanoparticles

The synthesis of FeMn oxide nanoparticles is carried out by thermal decomposition of iron pentacarbonyl, $Fe(CO)_5$ (Note that $Fe(CO)_5$ is a toxic liquid and should be handled in a well ventilated hood), and reduction of Mn(II) acetylacetonate, $Mn(acac)_2$, in a hot organic solvent with oleic acid and oleylamine as surfactants, using standard Schlenk line techniques under dry nitrogen gas protection. The organic solvent can be dioctyl ether, benzyl ether, octadecene, or mixture of these. Particle size can be generally controlled by simply adjusting the molar ratio of surfactants to precursors. The particle size is slightly bigger if 1-hexadecanediol is not used as a reducing agent. The size of the FeMnO nanoparticles will be further increased by decreasing the heating rate and increasing the intermediate reaction temperature. A schematic of the mechanism for colloidal growth and the resulting SEM showing the monodisperse nature of these nanoparticles is shown in **Figure 2**.

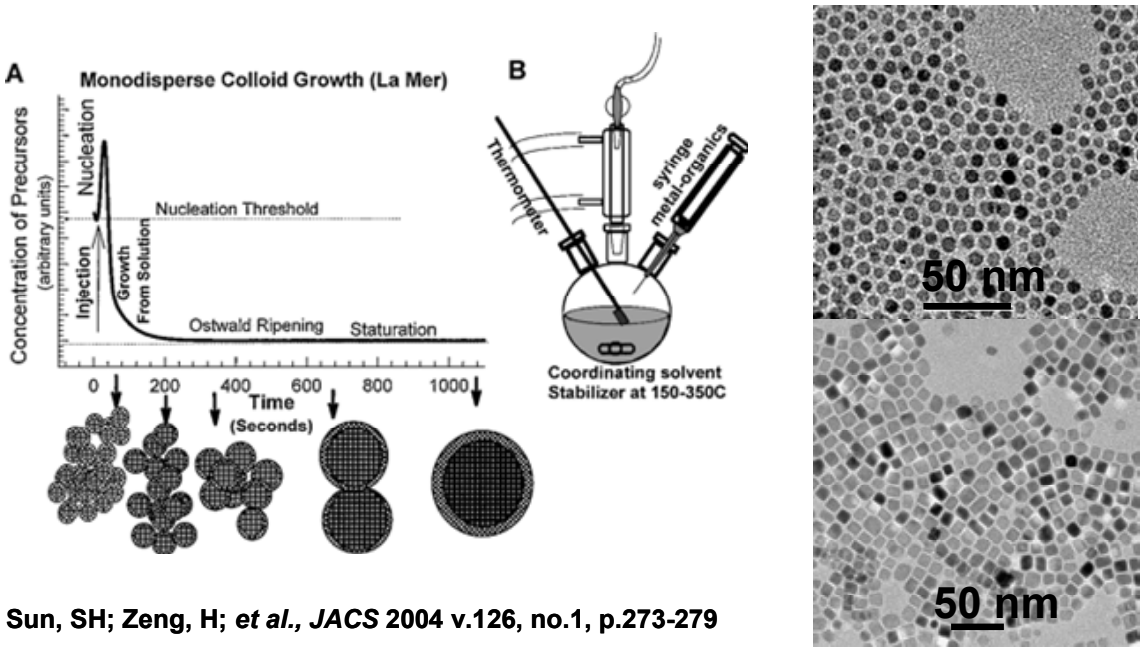

Sun, SH; Zeng, H; *et al., JACS* 2004 v.126, no.1, p.273-279

Figure 2: (A) The growth mechanism and the impact of time on the particle size. (B) Drawing of the generalized reaction set-up. SEM photos of the poly-dispersed nanoparticles obtained from this synthetic protocol.

3.1.1 *Synthesis of 12 nm FeMn Oxide Nanoparticles*

Under flow of nitrogen (~5mL/min), $Mn(acac)_2$ (0.5 mmol) was mixed with benzyl ether (10 mL) and heated to 100 °C. Under a blanket of nitrogen, $Fe(CO)_5$ (1 mmol), oleylamine (4 mmol), and oleic acid (4 mmol) were then added. The mixture was heated to 240^{o}C at a heating rate of ~15 °C/min., and incubated at this temperature for one hour to assure complete decomposition of $Fe(CO)_5$, and then heated to reflux (295~300^{o}C). The mixture was kept refluxing at this temperature range for 2 hours. During this time, slow nitrogen flow (~1mL/min) was introduced from time to time to remove some low boiling-temperature by-products and maintain the refluxing temperature between 295~300^{o}C. The reaction mixture was allowed to cool to room temperature by removing the heating source. FeMnO nanoparticles were precipitated out and washed twice with ethanol. The precipitates were re-dispersed in a 10 mL of hexane

with small amounts of oleic acid and oleylamine. Further centrifugation was used to remove any un-dispersible precipitates in the hexane. The final FeMnO nanoparticles are stored in hexane with small amounts of stabilizers (oleic acid and oleylamine). A similar procedure was used for the synthesis of the Fe_3O_4 nanoparticles.

3.1.2 *Preparation of Water Soluble Nanoparticles*

In a typical nanoparticle-micelle synthesis procedure, a concentrated suspension of nanoparticles in chloroform was added to an aqueous solution containing a mixture of surfactants or phospholipids. Addition of the nanoparticle chloroform suspension into the surfactant/lipid aqueous solution under vigorous stirring resulted in the formation of an oil-in-water micro-emulsion. Evaporation of chloroform during heating (40-80˚C, ~10 minutes) transfers the nanoparticles into the aqueous phase by an interfacial process driven by the hydrophobic van der Waals interactions between the primary alkane of the stabilizing ligand and the secondary alkane of the surfactant, resulting in thermodynamically defined inter-digitated bilayer structures surrounding each nanoparticle and form nanoparticle-micelles.

3.2 NMR Experimental Details

The solution state ^{1}H NMR spectra were obtained on a Bruker DRX400 instrument at an observed frequency of 400 MHz using standard conditions at room temperature and a 5mm double resonance probe. The chemical shifts were referenced to the secondary external standard TMS ($\delta = 0$ ppm). The spin-lattice relaxation time T_1 was measured using an inversion recovery pulse sequence, while the spin-spin relaxation time T_2 was measured using a Hahn echo. Both sets of data were fit using the Bruker software

XWINMR by integrating over the entire peak and fitting the exponential curves. For initial measurements, 1 μL of the superparamagnetic nanoparticles were added to 500 μL of DI H_2O. To study the effects of concentration, additional 2 μL aliquots of sample were added to the test tube, and the relaxation measurements were taken. The range of paramagnetic materials added was 1-11 μL. The tubes were shaken immediately prior to the relaxation measurements to ensure that the paramagnetic beads were not settled in the bottom of the test tube. The relaxivities were calculated by fitting the measured relaxation rates to Eqn. 2.4.

3.3 Particle Size Versus Relaxation

The spin-spin relaxation rate R_2 (= $1/T_2$) as a function of Fe concentration for the different superparamagnetic nanoparticles is shown in **Figure 3**. The spin-lattice relaxation rate R_1 (= $1/T_1$) as a function of Fe concentration for the different superparamagnetic nanoparticles is shown in **Figure 4**. The measured relaxivities are given in Table 1. Even though the sample selection is limited a few observations can be made. The $MnFe_2O_4$ nanoparticles show the highest relaxivity, but this can be attributed to the large nanoparticle size, plus the presence of Mn which is also paramagnetic. ICP (inductively coupled plasma) atomic adsorption analysis was used to determine the solution Mn and Fe concentrations. The Mn/Fe ratios observed by ICP experimentally for the $MnFe_2O_4$ nanoparticles were 1/1.37 and 1/1.57 for the 12.6 and 15.3 nm particles, respectively. This is significantly different from the 1/2 ratio predicted based on chemical formulation. This result demonstrates that the compositions of the synthesized nanoparticles were not the ratio formulated, and suggests a higher ratio of Mn

incorporation into the nanoparticles. The relaxivity rates can be corrected for the presence of Mn and are also given in Table 2. Following this correction for the measured concentration of Mn, the Fe_3O_4 CTAB modified superparamagnetic nanoparticle (8.4 mm) gave both the highest r_2 and r_1 relaxivity. A comparable C8 lipid modified nanoparticle gave a r_2 relaxivity that was ~2 times smaller, but analysis of this sample was difficult due to the very low concentration thus limiting the range of concentrations measured in the relaxation experiments. Part of this difference may arise from aggregation effects of CTAB versus C8 lipid, as this is also known to greatly influence relaxivity.

There is an initial increase in the relaxivity with increasing size for the $MnFe_2O_4$ nanoparticles, followed by a decrease in the observed r_2 and r_1 relaxivity above ~ 12 nm. This is in contrast to previous studies that show a steady increase in the relaxivity with increasing particle size through 15 nm [38]. Part of this discrepancy may arise from the observed frequency at which these experiments were performed (400 MHz versus 40 to 60 MHz). Our initial goal was to measure these relaxivities at the lower field strengths using the MAGRITEK console system described in Section 7, but this milestone was not completed prior to the ending of this project.

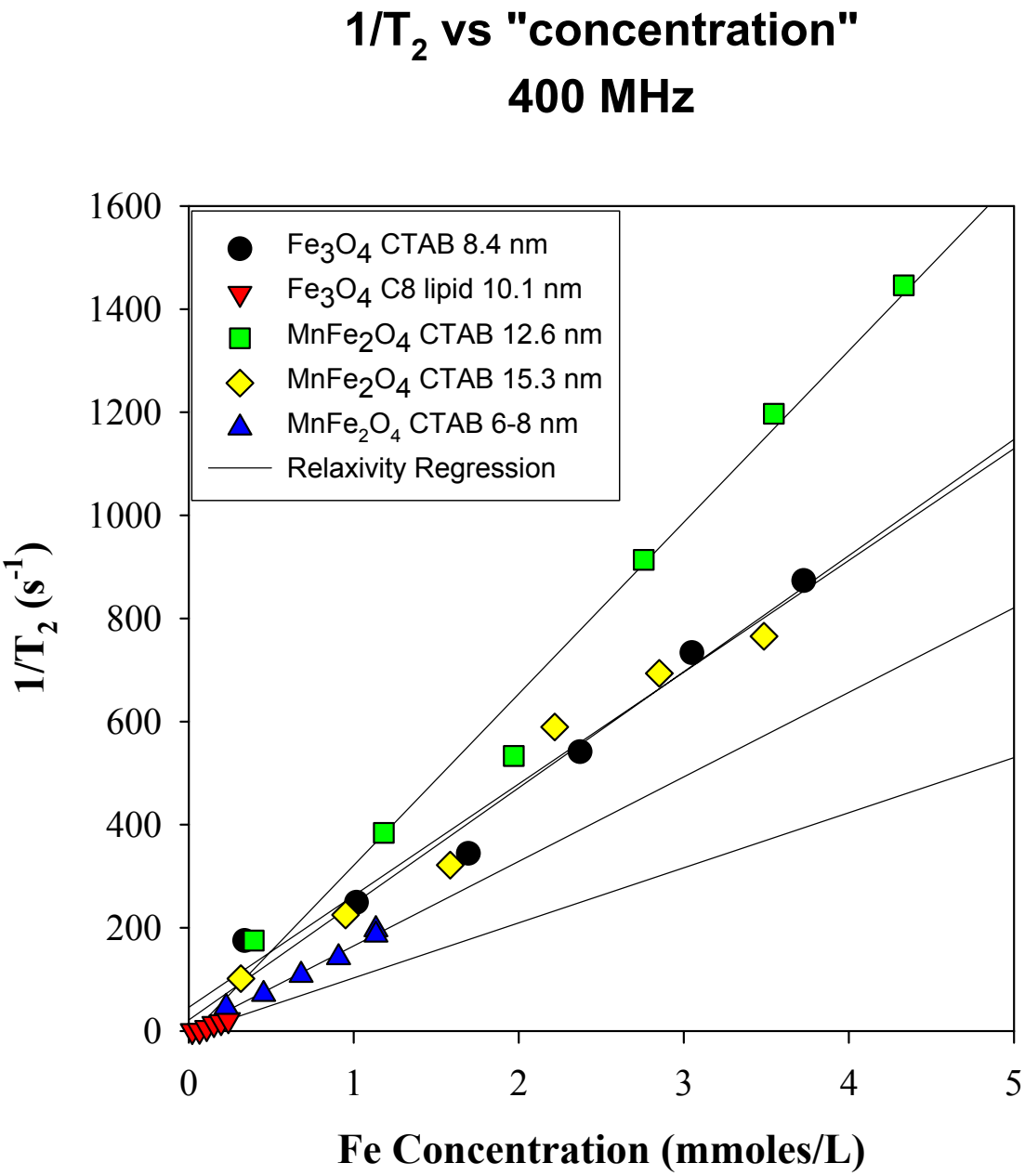

Figure 3: The variation of the water R_2 relaxation rate with concentration for a series of different superparamagnetic nanoparticles.

Table 1. Experimentally determined r_2 and r_1 relaxivity values for different superparamagnetic nanoparticles.

Sample	r_2 (s^{-1} mM^{-1} Fe)	r_1 (s^{-1} mM^{-1} Fe)
Fe_3O_4 CTAB 8.4 mm	216.7	0.99
Fe_3O_4 C8 Lipid 10.1 mm	106.8	~0[c]
$MnFe_2O_4$ CTAB 12.6 mm	332.7 (191.0)[b]	0.41 (0.24)
$MnFe_2O_4$ CTAB 15.3 mm	225.1 (129.6)[b]	0.86 (0.50)
$MnFe_2O_4$ CTAB[a] 6-8 mm	163.9	0.52

[a] Mn ratio not determined.
[b] Corrected for the combined Mn and Fe concentration as determined by ICP, units are s^{-1} mM^{-1} [Fe +Mn].
[c] Not well defined due to narrow concentration range investigated giving a negative relaxivity.

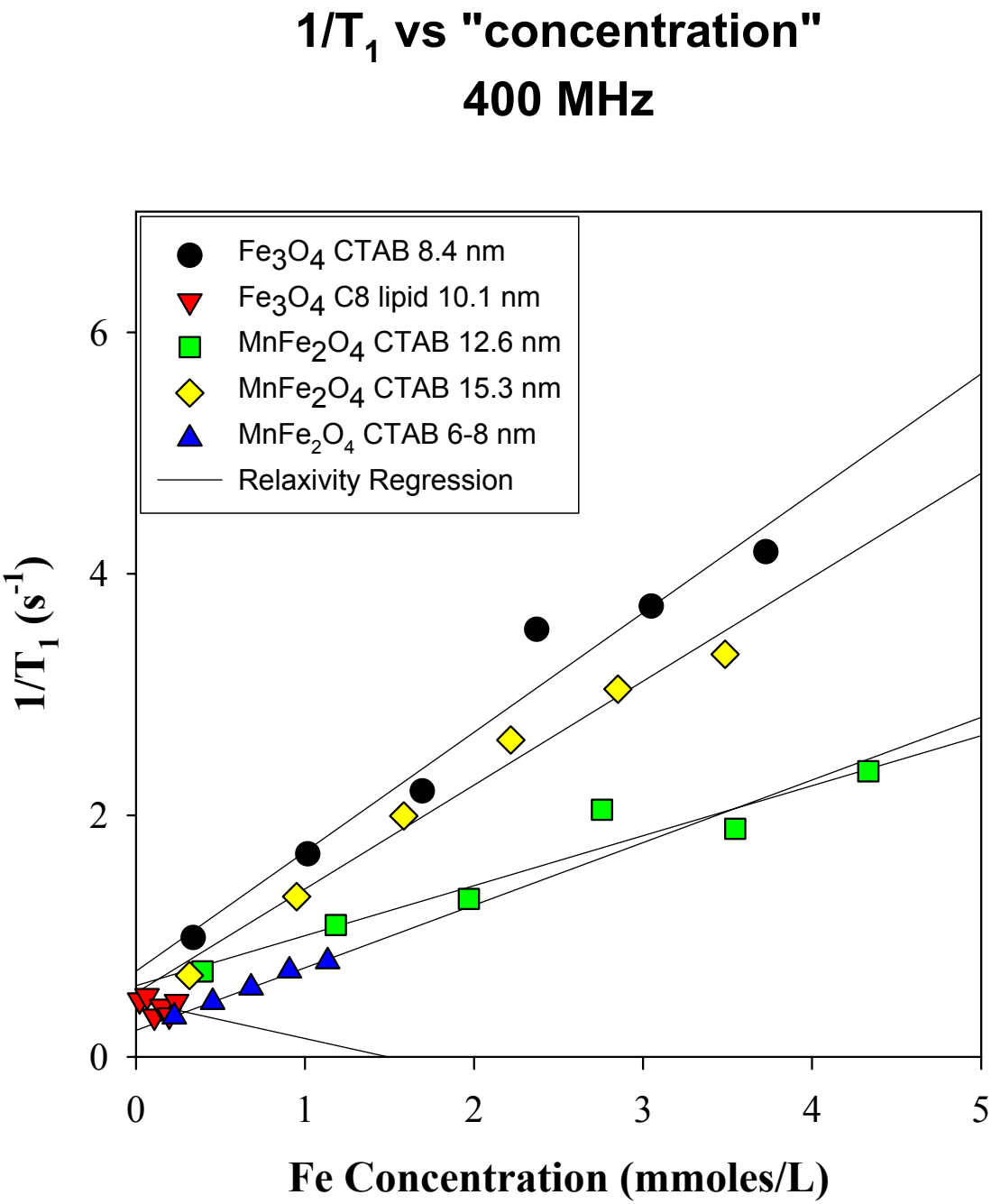

Figure 4: The variation of the water R_1 relaxation rate for a series of different superparamagnetic nanoparticles.

3.4 Impact on Project Nano-Detection Scheme

Based on these limited results it appears that superparamagnetic Fe_3O_4 nanoparticles should be employed as they give a higher relaxivity than the $MnFe_2O_4$ nanoparticles. These results also demonstrated that there is a high degree of variability in the Mn/Fe ratio with changes in particle size, suggesting a non-uniform precipitation event is occurring during the colloidal preparation of these nanoparticles. Unless this variation can be better controlled the utility of the mixed $MnFe_2O_4$ nanoparticles for quantitative detection work is highly questionable. Finally, one of the milestones for this project was the bio-conjugation of these Sandia prepared nanoparticles to anti-bodies. It was hoped that these smaller nanoparticles could be tested and compared to the larger commercially available SPIONs utilized in Section 6. Unfortunately, this work was not completed.

4. Solenoid Detection Coil Development

Under this LDRD program two separate μ-coil detection platforms were explored. The first (described here) is based on the most common solenoid coil design, but utilizes a unique production method. The second detection design utilizes a planar μ-coil, and will be described in Section 5. The final objective was to construct μ-coils where the detection volume was on the order of 100's of μm in order to optimize the effect of superparamagnetic nanoparticle relaxation.

4.1 Analysis of Coil Resistance and SNR for Thin Ribbon Wire[a]

The fabrication technique that produces the focused ion beam (FIB) solenoid μ-coil (details in section 4.2) utilized a metal plating process with very thin films. The film thickness greatly impacts the performance of the μ-coil, and raises some theoretical limitations (discussed in this section). When the dimensions of the wires of a coil operated at RF frequencies become large when compared to the skin depth, the resistance of the coil becomes much larger than one would expect based on the coil's cross-sectional area. The reason is that the eddy currents induced in the wire by the alternating magnetic field due to the RF current tend to force the current to the outer regions of the wire. Hence the area of the wire carrying current is reduced. At high frequencies, the current is effectively confined to a region within a skin depth of the wire surface.

Peck, Magin, and Lauterbur offer an analysis of micro-coils built with wires of circular cross-section [39]. The dependence of coil signal–to-noise (S/N) on design parameters such as the coil diameter and number of turns is given both in the limit of large wire diameter, appropriate for conventionally sized NMR solenoid coils, as well as

[a] This detailed analysis was provided by Andrew McDowell at New Mexico Resonance, Albuquerque, NM.

the limit in which the wire diameter becomes less than the skin depth (δ), a limit which can be approached with μ-coils. Peck, *et al.*, assume some geometrical constraints (coil aspect ratio of h/d_{coil} =1.5, coil spacing relative to wire diameter of s/d = 1.5), which may or may not be important for the ribbon wire coil. Hence, we extend their theoretical considerations.

The signal-to-noise ratio (SNR) per unit sample volume for a solenoidal coil of fixed aspect ratio (h/d_{coil}) in which the coil resistance is the dominant noise source can be expressed:

$$SNR \propto \frac{\omega_0^2 n / d_{coil}}{\sqrt{R_{coil}}} \tag{4.1}$$

The constraints of coil geometry, combined with the skin depth, result in the SNR with dependence on R_{coil}, n, d_{coil}, and ω_0, which are the coil resistance, number of coils, coil diameter and observed frequency, respectively. These dependencies change form as a function of wire size and shape. This allows us to ask: "Given a sample size and shape, how many turns should the coil have?" To place the ribbon wire results in context, we first summarize the circular wire results of Peck *et al.* [39].

4.1.1 *Small Wire Limit*

In the limit of small wires or large skin depth (d/δ <<1), the entire cross sectional area of the wire carries current. At a fixed aspect ratio (h/d_{coil}) and relative turn spacing,

the diameter of the wire must decrease as the number of turns of wire is increased. The coil resistance is given by

$$R_{coil} \propto \frac{n^3}{d_{coil}} \tag{4.2}$$

One power of n comes from the length of the wire, while the other two come from the decrease in cross-sectional area of the wire. Increasing d_{coil} serves to lengthen the wire, but also provides for an increase of the wire diameter since the overall length scale of the coil is increased. The expected signal-to-noise ratio is now given by

$$SNR \propto \frac{\omega_0^2}{\sqrt{n d_{coil}}} \tag{4.3}$$

which is the same as Eqn. [8] in Peck *et al.* [39].

4.1.2 *Large Wire Limit*

In the limit of small skin depth or large wire ($d/\delta >>1$), the circular wire only carries current in the region within one skin depth of its surface. Hence the effective cross-sectional area of the wire is reduced to $\pi d\delta$, which yields a coil resistance given by

$$R_{coil} \propto n^2 \xi \sqrt{\omega_0} \tag{4.4}$$

where ξ is used to account for the proximity effect, in which eddy currents due to the flux from neighboring wires contribute to the redistribution of the current. One expects $1 < \xi < 3$, roughly. The dependence on ω_0 comes from the skin depth. The dependence on n and d_{coil} is reduced from the small wire result (Eq. 4.2) because a reduction in the wire diameter has a smaller impact on the effective cross-sectional area than for the small-wire case. The corresponding SNR equation is

$$SNR \propto \frac{\omega_0^{7/4}}{d_{coil}\sqrt{\xi}} \tag{4.5}$$

4.1.3 *Ribbon Wire, Intermediate Limit*

A flat ribbon wire allows an intermediate situation, in which the skin depth is small compared to the wide dimension but large compared with the thin dimension. At an observed frequency of 44.6 MHz, the skin depths of copper and gold are 10 μm and 12 μm, respectively. Hence, the proposed ribbon of dimensions 45 μm x 5 μm falls into the intermediate limit. In this limit, the current will be confined to a region of width δ near the edges of the ribbon. If we let τ be the thin dimension, the effective cross sectional area of the wire is $2\tau\delta$, yielding a coil resistance of

$$R_{coil} \propto \frac{n\, d_{coil}\xi\sqrt{\omega_0}}{\tau} \tag{4.6}$$

Since the width of the ribbon has no impact on the effective area in this limit, the influence of either n or d_{coil} is "reduced" even below that of the small circular wire case. The corresponding signal-to-noise equation is

$$SNR \propto \frac{\omega_0^{7/4}\sqrt{n\tau}}{\left(d_{coil}\right)^{3/2}\sqrt{\xi}} \tag{4.7}$$

4.1.4 *Ribbon Wire in the Small Wire Limit*

As the ribbon width (w) is reduced, eventually the skin depth is less than $w/2$. In this limit, the entire wire once again carries current. In this case, the effective cross sectional area is simply τw. In this limit, the width of the ribbon wire is inversely proportional to the number of turns, for fixed coil length. Hence the resistance is

$$R_{coil} \propto \frac{n^2\, d_{coil}}{\tau} \tag{4.8}$$

We have dropped reference to the proximity effect factor ξ under the assumption that current already spread across the wire will not be significantly moved by flux from neighboring turns. This yields

$$SNR \propto \frac{\omega_0^2\sqrt{\tau}}{\left(d_{coil}\right)^{3/2}} \tag{4.9}$$

Note that this result is comparable to the LARGE wire limit not the small wire limit for round wire. The reason for this apparent discrepancy is that the cross sectional area for the ribbon is inversely proportional to *n*, just as in the large (round) wire limit. Note that it is possible to reach the narrow wire limit without having wire width *w,* be inversely proportional to the number of turns. Such a coil would have a large turn-to-turn spacing (and weak proximity effect). In this case the resistance would be given by

$$R_{coil} \propto \frac{n\, d_{coil}}{\tau w} \tag{4.10}$$

This yields

$$SNR \propto \frac{\omega_0^2 \sqrt{n\tau w}}{\left(d_{coil}\right)^{3/2}} \tag{4.11}$$

This result indicates that such a coil is poorly engineered, at least from a signal to noise perspective; the SNR could be increased by increasing either *n* or *w* so that there is not so much excess space between turns.

4.1.5 *Implication for Coil Design*

In Peck [39], the coil aspect ratio *(h/ d_{coil})* and turn-to-turn spacing (*s/d*) are held fixed, both at a value of 1.5. For the ribbon coil in the intermediate limit, there is no reason to impose the turn spacing limit, aside from considerations that closely spaced turns might boost the strength of the proximity effect (i.e., the value of ξ). Assuming that we will build a ribbon coil that does not violate the spirit of these constraints, we might directly compare the above results:

Table 2. SNR variation for coil design limits.

Limit	***SNR* Dependence**
Small wire ($d << \delta$)	$\frac{\omega_0^2}{\sqrt{n d_{coil}}}$
Large wire ($d >> \delta$)	$\frac{\omega_0^{7/4}}{d_{coil}\sqrt{\xi}}$
Ribbon (intermediate limit)	$\frac{\omega_0^{7/4}\sqrt{n\tau}}{(d_{coil})^{3/2}\sqrt{\xi}}$
Ribbon (small wire limit)	$\frac{\omega_0^2\sqrt{\tau}}{(d_{coil})^{3/2}}$

The ribbon wire in the intermediate size limit encourages maximizing the number of turns, while the small wire limit encourages a low number of turns. The microcoils built for the experiments of Peck, et al. [39], had only 5 turns. Note that the benefit of

minimizing the coil size scale is larger for the ribbon coil than for the other types. The above equation describes the benefits of maximizing the number of turns for a ribbon coil up to the limit when the ribbon wire width becomes only a few skin depths. Beyond that limit, increasing the number of turns requires decreasing the width. In this case, the ribbon is no longer in the intermediate limit, but is more like the large wire. In a similar vein, the thickness of the ribbon can be increased up to a limit set by twice the skin depth before the intermediate limit is breached. In this case, additional thickness has no impact on the coil performance, since adding ribbon thickness can be done without changing *n*.

It would appear that the optimal ribbon geometry would be a thickness $t \leq 2\delta \approx 20\mu m$ and a width of $w \geq 2\delta \approx 20\mu m$.

4.2 Fabrication Details

The solenoid μ-coils were fabricated [40] onto 2.5-cm long quartz tubes (Vitrocom, Mountain Lakes, NJ) having a 550 μm outer diameter and 400 μm inner diameter using the procedure depicted in **Figure 5**. These coil dimensions will commonly be denoted as 550/400. Each tube was cleaned using hydrogen peroxide followed by acetone and isopropyl alcohol. After wet chemical treatment, the tubes were masked on each end, and the 6.2 mm unmasked center targeted for metal deposition was etched for 15 min using an 100 W O_2/Ar plasma. The central region length was chosen based on the coil design with two 2-mm long cuffs on either end. The masked tubes were mounted into individual pin vice fixtures for metal deposition. A stage having eight individual rotation stations contained within a high-vacuum thin film deposition chamber allowed for simultaneous coating of multiple tubes at a constant working distance of 35 cm. Electron

beam evaporation was used to deposit a thin Cr layer (200 Å) followed by a relatively thick Au layer (5 μm) around the circumference of the tubes. Deposition rates were chosen to minimize the stress in the layers. After removal of the tubes from the deposition system, the masks were removed using acetone, and the tubes were re-mounted into pin vice fixtures for rotation within the focused ion beam (FIB) system. Thirty keV Ga ions emitted from a liquid metal ion source were used to remove the Au/Cr layer in order to define the coil and the neighboring cuffs. The ion beam was focused to a width of approximately 0.5 μm using a dual-lens Magnum ion column (FEI Co., Hillsboro, OR) and steered across areas outlined by the operator until all the metal was removed from targeted regions. Rates of metal removal were on the order of 10 $\mu m^3/s$ when using a 20 nA Ga beam. Minimal heat and force accompany FIB bombardment. The secondary electron intensity was monitored during ion bombardment to ensure complete removal of metal and slight penetration into the quartz. An example coil is shown in **Figure 6A** with areas removed by the FIB appearing relatively dark due to the low secondary electron intensity. As indicated in **Figure 5**, step 4, and the schematic in Figure 6B, the sample was rotated by an in-vacuum, single-axis rotary stage and translated by a high precision x–y stage along the tube axis in order to define a helix [40]. The motion-control system, consisting of an ultra-high vacuum compatible stepper motor (controlled by a Princeton Research Instruments stepper motor unit) and a reduction gear assembly, could orient a sample with 0.25^o precision. This FIB method could likely be extended to fabricate coils onto much smaller tubes having <50 μm OD. The finished metal coil used in this initial 550/400 coil (**Figure 6C**) had 28 turns over a length of 2.1 mm. The coil conductors were 65 μm wide with a gap between turns of 10

μm. The sample detection volume within the NMR microcoil was 264 nL. The filling factor was $(400/550)^2 = 53\%$. On the 2-mm long metal cuffs, the FIB removed a 10-μm wide line parallel to the tube axis in order to interrupt conduction. The secondary electron detector within the FIB system also enabled registration of the coil turns. The direct current resistance (Fluke model 179) of the coil was found to be 5.42 Ω. The resistivity of our evaporated Au is 2.898 $\mu\Omega$-cm (measured on a flat substrate), somewhat higher than bulk Au. Using this value and the geometry of the coil, we calculate a DC resistance of 4.3 Ω. This differs from the measured resistance, perhaps due to contact resistance in the silver epoxy used to attach the coil to the circuit board. The microcoil inductance was calculated to be 93 nH.

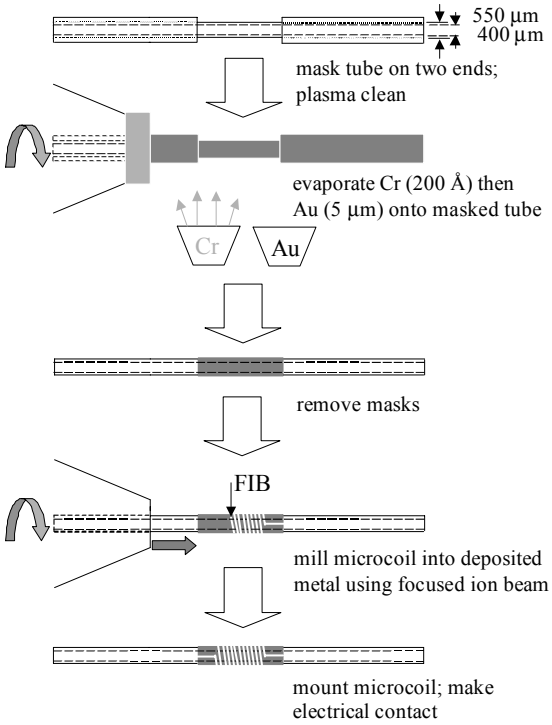

Figure 5: The sequence of steps used in the fabrication of the solenoid NMR µ-coil.

The coil was packaged using DuPont Green Tape Low Temperature Co-Fired Ceramic (LTCC) material (DuPont Microcircuit Materials, Research Triangle Park, NC) upon which alloyed gold (Pt/Au) co-fireable material (DuPont 5739) solder leads had been plated (Figure 6D). The coil was secured to the leads, above an opening in the substrate, by means of silver epoxy. This opening assured that the microcoil did not contact the supporting platform and prevented distortion or damage to the very thin metal layer. Mounting the microcoil on a substrate also allowed us to safely manipulate the coil and to attach a fluid transfer line.

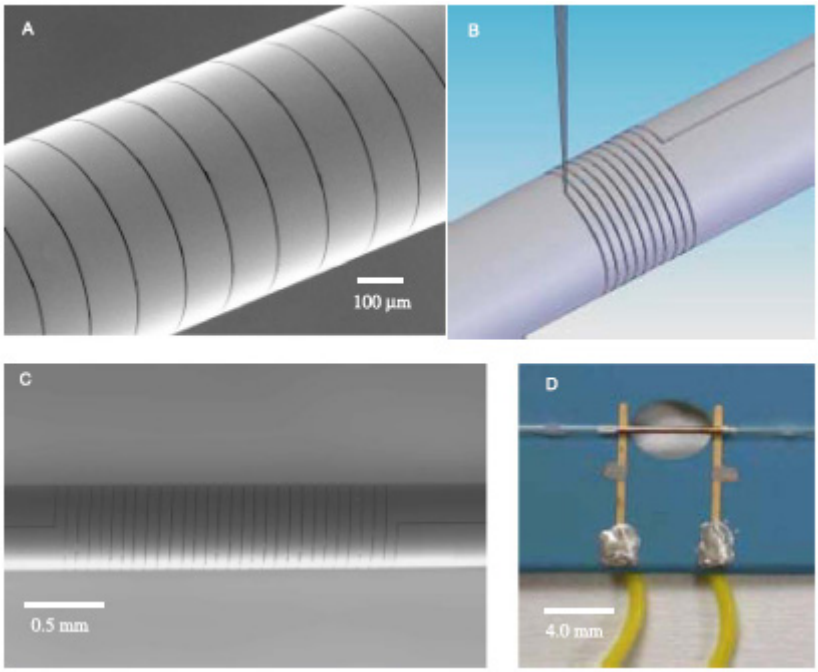

Figure 6: Focused ion beam lathe machining of the NMR microcoil. (A) Scanning electron micrograph of a coil during the machining process. (B) Schematic of the Ga ion beam machining process. (C) SEM of the coil tested in this work. (D) The finished NMR l-coil mounted on a low temperature co-fired ceramic substrate with electrical connections.

In addition to this 550/400 µ-coil, two other coils were fabricated using similar procedures described above. The coils were fabricated on a 175 µm OD fused quartz capillary with an inner ID of 100 µm (175/100). The first coil utilized a 60 µm conductor width, 10 µm insulator width to give a 10 turn coil. The second 175/100 µ-coil utilized a 30 µm conductor width, with a 10 µm insulator width to give a 16 turn µ-coil. The predicted resistance for these µ-coils was 0.52 and 1.6 Ω, respectively.

4.3 Micro-Coil Tuning Circuit

Although the 93 nH inductance of the microcoil could reach resonance at 44.2 MHz with a variable capacitor of reasonable size, we plan to work with much smaller

coils in the future. Such small coils are typically operated at higher frequencies [15], where directly resonating the small inductance is feasible. This will not be an option for smaller coils at 44.2 MHz or less, a fact that motivated us to seek alternative ways of tuning the microcoil.

Our tuning solution was to build an auxiliary tank circuit with conventional scale capacitors and to connect the microcoil to it. The key parameter of our microcoil that guided the design of this tuning circuit was its very high resistance. Optimization of a coil's SNR is a compromise between maximizing coil efficiency, in terms of the magnetic field produced at the sample per unit current in the coil, while minimizing the resistive noise. The dominant noise source for our very thin, ribbon-wire coils was the large coil resistance [39]. Therefore, the introduction of the inductor did not degrade performance, *because this extra inductance did not contribute to the losses.* Our microcoil made such a small contribution to the resonant inductance that its function was really that of a resistor.

We, therefore, constructed two circuits for our experiment (**Figure 7**). In both cases, the microcoil was mounted by itself in a cast aluminum box, while the external tuning inductor and tuning and matching capacitors were mounted in a separate aluminum box. In the first circuit (**Figure 7a**), we used a quarter-wave cable to transform the coil resistance to a higher value and then placed this transformed impedance in parallel with the tuning inductor. In this case, the full resonant voltage was applied to the (transformed) sample coil impedance. In the second circuit (**Figure 7b**), the sample coil and tuning inductor were in series, so that all of the resonant current flowed through the sample coil.

The two circuits exhibited nearly identical SNR performance. All subsequent measurements were performed with the first circuit (**Figure 7a**), because the remote placement of the tuning and matching elements made it more convenient to work with. The external "tuning" inductor in this circuit was 5 turns of 14 gauge bare copper wire, with a calculated inductance of 0.25 μH, and a calculated resistance at 44.2 MHz of 0.07 Ω. The tuning and matching capacitances were both ~22 pF. The large value of the matching capacitance resulted from the high losses in the microcoil. Because our Wavetek radio frequency sweeper operates at the mW level, and we were reluctant to subject our coil to this power, we estimated the Q of the resonant circuit by constructing a mockup of the microcoil using robust 36 gauge copper wire and a 5 Ω resistor. The mockup circuit had a Q of about 10, as measured from the half-power points on the sweeper output. We also calculated the Q of the coil based on its D.C. resistance, calculated inductance, and resonance frequency ($Q = \omega L/R$) which gave a similar Q value of 5.

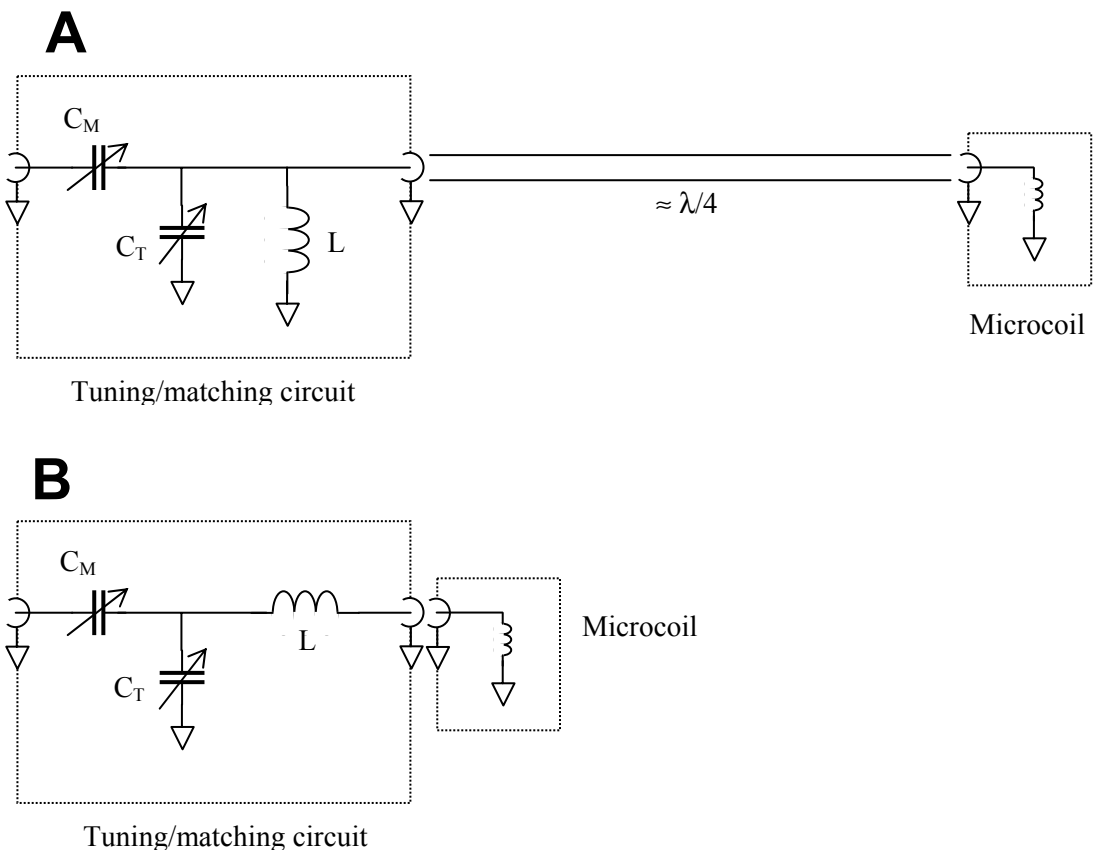

Figure 7: Tuning and matching circuits for low-inductance sample coils at low frequency.

4.4 Low-Field NMR Experimental Details

The ^{1}H NMR measurements, at a resonant frequency of 44.2 MHz, were performed using a MRTechnology (Tsukuba City, 300-2642 Japan) console, interfaced to a 1.04 Tesla NEOMAX permanent magnet developed for small animal MRI, but a suitable smaller magnet could be fabricated to be used with the microcoil set up. This system resides at New Mexico Resonance, Albuquerque, NM. The implementation of a second micro-NMR console utilizing a MAGRITEK system and a 0.96 Tesla magnet at Sandia National Laboratories is described in Section 7. The transmitter pulses were output directly from the console, without a conventional radiofrequency power amplifier

because only 0.25 mW of power was required to produce a B_1 field of 0.3 Gauss (*vide infra*). Liquid samples were imbibed directly into the coil form. Ethanol (100 %) was purchased from AAPER (Shelbyville, KY).

4.5 Low-Field NMR Testing of Solenoid Micro-Coil [b]

The magnetization nutation performance of the solenoid μ-coil is shown in **Figure 8**, where the signal intensity, after an excitation pulse, from a sample of de-ionized water, is plotted as a function of pulse width α. The data followed a typical sin(α) curve, indicating uniform sample excitation by a homogeneous RF field. The π-pulse width, determined from fitting the sine curve, was 397 ± 4 μs. The transmitter amplitude was 0.32 V (peak-to-peak), corresponding to a power into 50 Ω of only 0.25 mW. A π/2-pulse time of 200 μs corresponds to an RF field strength of 0.3 G (or 1.25 kHz), which is produced in our coil by a current of 1.8 mA.

[b] This work has recently been published, Laurel O. Sillerud, Andrew F. McDowell, Natalie L. Adolphi, Rita E. Serda, David P. Adams, Michael J. Vasile, Todd M. Alam, "^{1}H NMR Detection of Superparamagnetic Nanoparticles at 1T Using a Microcoil and Novel Tuning Circuit", *J. Magnetic Resonance*, **181** (2006), 181-190.

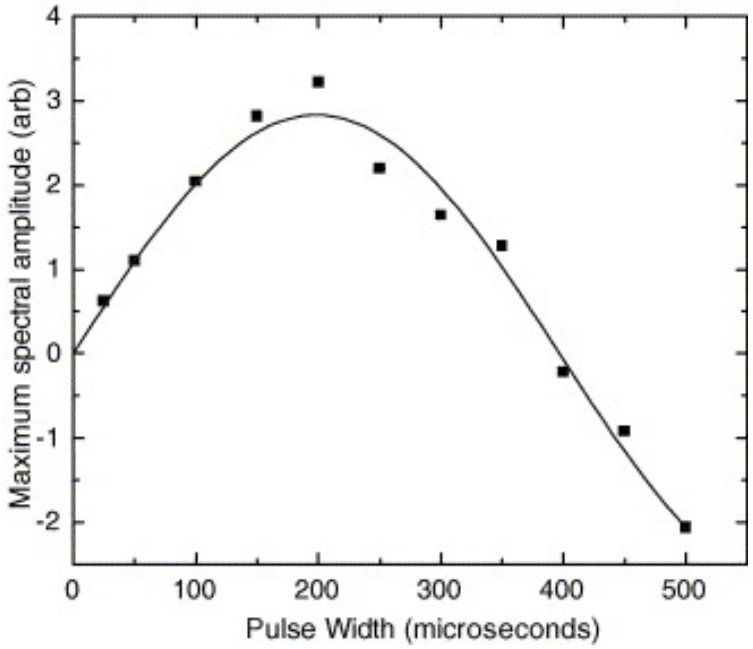

Figure 8: Determination of the π-pulse width in the μ-coil from a water sample.

The free-induction decay (FID) and spectrum of de-ionized (DI) water in the microcoil are shown in **Figure 9**. The spectrum has a full-width at half maximum (FWHM) of 2.5 Hz (0.056 ppm) and is reasonably well-fit by a Lorentzian, as shown in the left inset. (At 55% and 11% of maximum, the widths are 2.3 Hz and 8.7 Hz, respectively.) The SNR after a single π/2 pulse was found to be 137 (ratio of FID amplitude to rms baseline noise). The small sidebands at ±60 Hz were presumably due to gain modulations in our receiver amplifiers, caused by 60 Hz ripple. (Sidebands ±120 Hz were also observed.) **Figure 10** shows the NMR spectrum of a sample of 100% ethanol, calculated from 64 FIDs acquired with a 5 s repetition time. Peaks are seen at δ = 1.2, 3.7, and 5.5 ppm, corresponding to the CH_3-, -CH_2-, and -OH protons, respectively, with the correct relative amplitudes of 3:2:1 (Table 3). Note also that we can observe the ~7 Hz *J*-coupling for the methyl group, and the smaller couplings for the methylene and hydroxyl protons, indicating that the frequency drift over the 5-min experiment was <3 Hz. For

both the water and the ethanol experiments, only the *X*, *Y*, and *Z* gradients were shimmed because higher order shims were not available.

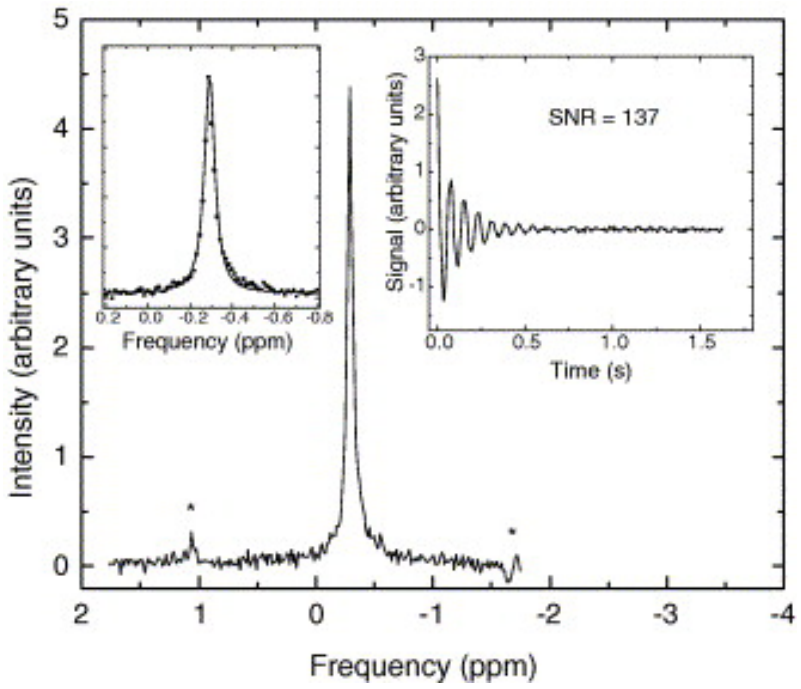

Figure 9: Absorption ^{1}H NMR spectrum of a sample of de-ionized water from the 550 μm OD μ-coil.

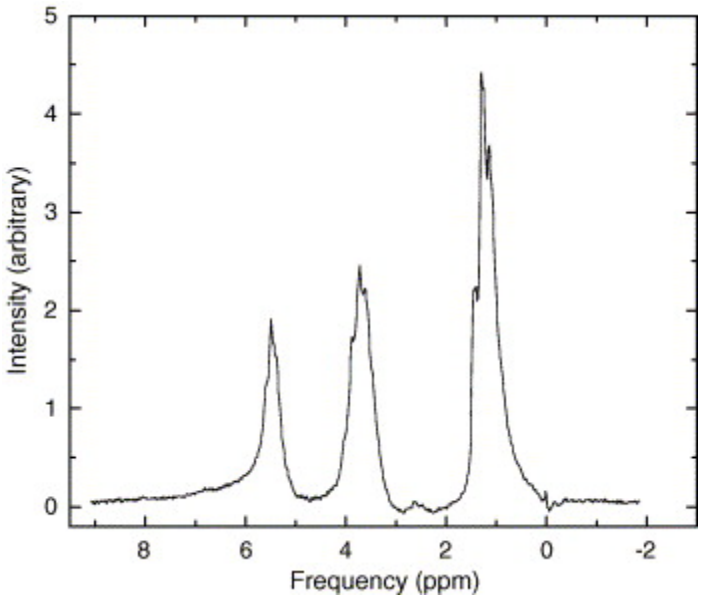

Figure 10: A ^{1}H NMR spectrum of 100% ethanol taken using the 550/400 solenoid μ-coil.

Table 3. Fit of the ethanol spectrum in the 550/400 solenoid μ-coil to the sum of three Gaussians.

δ(ppm)	Multiplicity	Amplitude
1.2 [1.2]*	[3]	3.0 [3]
3.70 [3.65]	[4]	1.9 [2]
5.48 [5.275]	[1]	1.1 [1]

*The standard values are shown in square brackets

In addition to these NMR results for the 550/400 solenoid μ-coil, experiments were also attempted on the 175/100(A) and 175/100(B) solenoid μ-coils. Even though the fluid handling and electrical connections to these smaller μ-coils worked well, no NMR signal was detected for the 175/100(A) μ-coil. One reason for this is that the sample volume in the new coils is about 1.9% of the sample volume of the 550/400 coil. This means that we should expect a signal-to-noise ratio of 2.6, all other things being equal. Unfortunately, this SNR will only be achieved with a receiver bandwidth of

approximately 312 Hz, and a very uniform magnetic field. These requirements make finding the resonance very difficult, and we did not see a signal. The double-pitch 175/100(B) coil should have twice the sensitivity of the 175/100(A) coils. In experiments with this coil, we also added a new audio filter to our apparatus so that we could achieve reliable filtering down to 125 Hz bandwidth. In tuning up this new coil, we noted that the electrical resonance was broader than expected. The reason for this is that the coil has a high resistance, even at DC. This resistance is about 3 times higher than calculated from the coil geometry. It turns out that ALL the tube-based coils have this same defect, which seriously compromises their performance as NMR detectors. We did not succeed in seeing a signal with the double-pitch 175/100(B) coil, even with careful filtering and searching for the resonance. We attribute this to the high resistance of this coil, which leads to high noise levels that obscure the small signal that we expect. We cannot be sure of the source of the high resistance, since we cannot make our own contacts to the tube-based coil itself, owing to its fragility. However, the fact that both 550/400 coils and 175/100 coils both show a factor of 3 enhancement in their resistance seems to implicate the plated metal layer out of which the coils are formed.

4.6 Impact on Micro-NMR Development

These results show that while these FIB fabricated NMR μ-coils can be used to obtain results they have several limitations. The primary limitation is the high resistivity observed in the μ-coils, which is ~ 3 times higher than that expected theoretically. This high resistance severely degrades the performance of the μ-coils, and has resulted in the inability to detect signal at the smaller coil dimensions. This clearly shows that the film thickness for these type of coils needs to approach two times the skin depth thickness (2δ

~ 20 μm) to regain the performance. Couple this resistance issue with the complexity of this fabrication technique and this detection platform does not appear to be one that should be readily pursued. If a method could be developed for easy fabrication of solenoid μ-coils with thick wire thickness, then this design would need to be re-evaluated.

5. Planar Spiral Micro-Coil Development

The second NMR μ-coil detection platform investigated was a spiral planar coil configuration. This type of coil has been studied extensively by other groups, and lends itself well to lithography-type fabrication.

5.1 Fabrication Details

An Archimedes coil was chosen to provide as much uniformity as possible for a 2-D design. However, most MEMS spirals require front side connections and an imbedded lead from the inner most winding. Both of these limitations reduced the effectiveness of placing a highly uniform coil as close as possible to an NMR sample with unknown geometry. The close proximity of the embedded conductor, typically a few microns, provides asymmetrical induction in the coil. Also, the placement of electrical leads on the front side reduces the geometrical space allowed for operation. A choice was therefore made to provide backside connections so that the inductor could be brought as close to any NMR sample as possible without unnecessary geometrical limits. Coils were manufactured on alumina substrates with Au/W filled vias purchased from Micro Substrates Corporation. The substrates purchased were 500 μm thick, which is sufficient to eliminate inductive effects from the electrical traces on the backside. Vias were

roughly cylindrical with a 75 µm diameter and a minimum pitch of 150 µm and provided through wafer electrical connections to each side of the coil. A diagram detailing the process steps required to produce the NMR induction coil is presented in Figure 11. A metal seed layer was then evaporated onto the bottom side of the substrate prior to spin casting with 75 µm of NFR-015 resist. After patterning, gold was plated into the resist mold to a thickness of 61 ± 1 µm across the entire four inch wafer. After electroplating, the patterned surface was coated again with negative photoresist and flood exposed to protect the backside of wafer during the remaining processing steps.

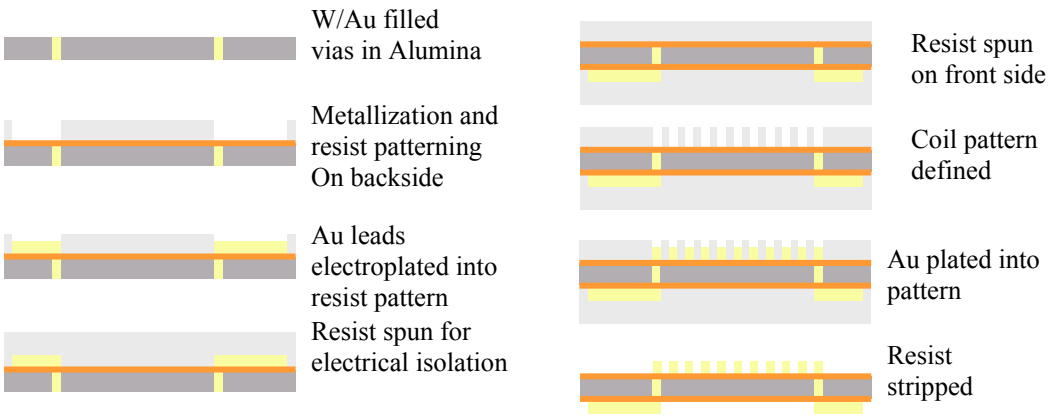

Figure 11: Process diagram for production of planar spiral NMR µ-coils.

Next, the top surface of the substrate was coated with a metal seed layer and 75 µm of NFR-015 resist. The resist was oven baked on a chuck holding the substrate at the edges, suspending the substrate in air to protect the resist underneath. Gold was plated into the resist mold after patterning to generate the induction coil. The backside of the substrate was protected against further plating by additional layer of photo-resist. Again, the

thickness and uniformity of the electroplated gold were measured to be 61 ± 1 μm across the wafer.

After plating, the photoresist was stripped and the metal seed layer was etched to complete the coils. **Figure 12** shows scanning electron micrographs of the top and bottom side of the substrate. A single isolated coil is shown in the top surface. Metal vias in the substrate provide contact between each end of the coil and its respective electrical contact on the backside. The Au/W via shown in **Figure 12** (a) is cylindrical in shape and makes contact with the end of the coil. Dimples seen in **Figure 12** (b) indicate the locations of the embedded vias underneath each lead.

(a) 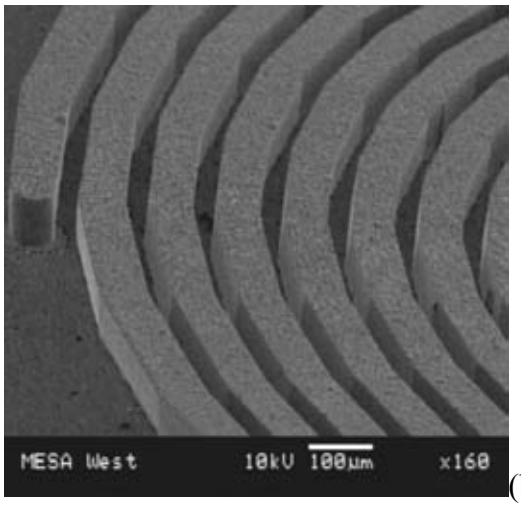

(b) 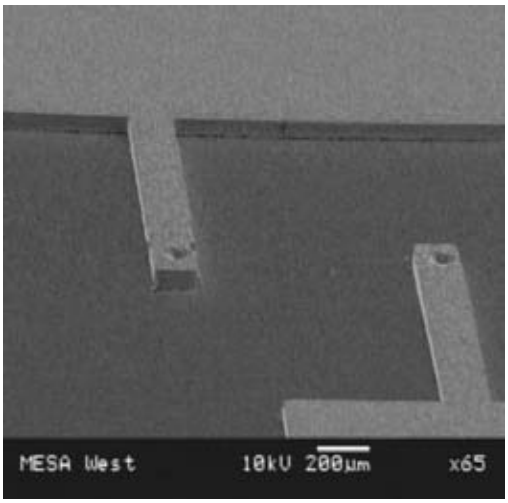

Figure 12: Gold induction coil on alumina substrate (a) Spiral coil with through wafer via contact at the end. (b) Backside electrodes with dimples in the electroplated metal directly over the metal vias.

Figure 13 shows a photograph of a 15 turn spiral coil demonstrating the uniformity of the spacing and wire thickness. Note that the coil wires are not perfect smooth arcs, but are

closely linked linear sections (this can also be seen in **Figure 12**) resulting from the initial design program. In addition to these circular coils a series of square μ-coils were also fabricated (see **Appendix 1**). A finite element analysis of the B_1 field produced by these square μ-coils showed a very non-uniform excitation profile with nodes present at each corner. For this reason testing of these square μ-coils was not pursued.

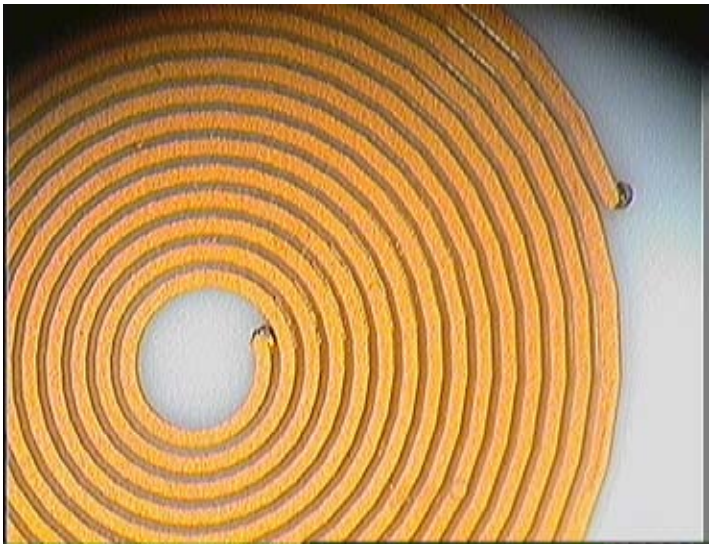

Figure 13: Photograph of a 15 turn circular planar spiral μ-coil.

The performance of these planar μ-coils is controlled by several design features. These include the width of the wire, the spacing between wires, the height of the wire and the number of turns. The inter-relationship of these different parameters on the SN performance of these μ-coils is complex. In **Appendix 2** a detailed analysis of the calculated performance for the different production parameters in presented. The two constraints imposed for this analysis were an operating frequency of 44 MHz, and an excitation volume within the center of the planar coils of ~ 500 μm for comparison to the coil dimensions of the solenoid μ-coil in Section 4. The initial coils produced have coil

line widths of 60 and 70 μm, with line spacings varying between 20, 30 or 40 μm and a wire height of 60 μm. Coils with 3, 7, 10, 12 and 15 turns were produced.

A short comment on reproducibility in the μ-coil is warranted. For the initial 57 spiral μ-coils delivered the DC resistance was measured, with a summary presented in **Appendix 3**. Approximately 11% of these coils showed an open circuit (high resistance), with all of these failures determined to be between the vias and the surface coil itself. This suggests that the through-via process could be improved for better reproducibility. The average DC resistivity, and standard deviation (σ) measured for the 3 turn μ-coils was 50 $m\Omega$ and $\sigma = 7$ $m\Omega$, for the 7 turn μ-coil was 189 $m\Omega$, with $\sigma = 66$ $m\Omega$, for the 12 turn μ-coil was 411 $m\Omega$, with $\sigma = 81$ $m\Omega$, and for the 15 turn μ-coil was 552 $m\Omega$, with $\sigma = 50$ $m\Omega$. This reveals that the standard deviation in the measured resistance varied considerably from 10% to as high as 30%.

5.2 Low-Field NMR Testing of Planar Spiral Micro-Coils

The experimental details for testing of the planar μ-coils was similar to that for the solenoid μ-coils described in Section 4.1, and will not be reproduced here. The samples were placed in a 500 μm/400 μm (OD/ID) capillary, and placed in the center of the spiral μ-coil. **Figure 14** shows the NMR spectrum for a planar 15 turn spiral μ-coil. The resolution is excellent, with the J-coupling between the different protons well resolved. This can be compared to the ethanol spectrum shown in **Figure 10** for the solenoid coil. These initial results show that the S/N and resolution are comparable between the different detection platforms.

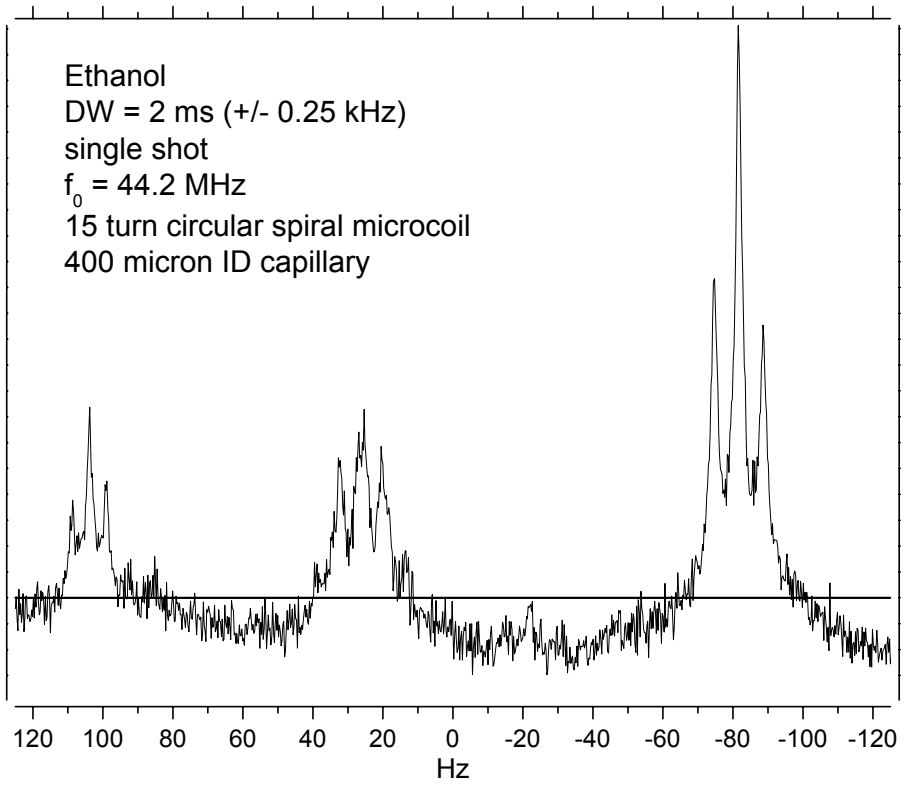

Figure 14: The ^{1}H NMR spectrum of ethanol obtained using a 15 turn planar μ-coil.

Different circular coil configurations were tested and are summarized in Table 4. The S/N ratio obtained for these planar μ-coils is ~3 times higher than that observed for the solenoid μ-coil in Section 4. There does not appear to be a significant change in the observed performance with changes in the number of coils used in the design. (Note the 3- turn coil results cannot be directly compared since a doped water sample was used for these initial tests). Additional characterization of these planar μ-coils will be performed in the future.

Table 4: Summary of performance results obtained for a series of planar spiral μ-coils.

#-Turns	Sample	Q	π/2 (μs)[a]	SNR, BW(Hz)[b]	FWHM (Hz)[c]
15	Ethanol	16	75	310 (± 500 Hz)	1.6
10	DI	25	65	420 (± 125 Hz)	1.2
7	DI	27	62	360 (±250 Hz)	2.5
3	Doped	30	--	47 (±1000 Hz)	~15 Hz

[a] Ninety degree RF pulse length.
[b] SNR = signal to noise ratio, BW = band width or filter width.
[c] FWHM = Full width at Half Maximum line width.

5.3 Impact on Micro-NMR Development

These results are encouraging and show that a high level of S/N and narrow line widths can be obtained using these planar spiral μ-coils. The ability to produce these μ-coils using existing lithography techniques is promising for future integration with other micro-devices and delivery systems. The one draw-back is the requirement for the coil to be perpendicular to the field direction, imposing a size limitation of the gap size in the magnet. Presently the die cut, and designed electrical connection pads for these μ-coils impose a 5 mm size limitations. Future fabrication runs could reduce this size maximum to a few mm without much effort. This will be the NMR μ-coil detection platform that we pursue for future development in the micro-NMR efforts here at Sandia.

6. Demonstration of SPION Detection

In addition to the relaxation experiments on small superparamagnetic nanoparticles described in Section 3, we also pursued investigations of commercial magnetic beads or superparamagnetic iron oxide nanoparticles (SPIONs). The question we wanted to pursue was what detection limit and amplification could be measured by observing the changes in the water relaxation of solutions containing SPIONs. These commercial SPIONs are readily obtained, already well characterized, very uniform, and have surface modifications already designed for bio-conjugation. Our initial demonstration utilizes the Dynabeads (MyOne Streptavidin) purchased from Dynal Inc. These beads (shown in Figure 15) are composed of thousands of 8 nm SPION uniformly dispersed in a polystyrene matrix, coated with a thin layer of polymer and a monolayer of streptavidin.

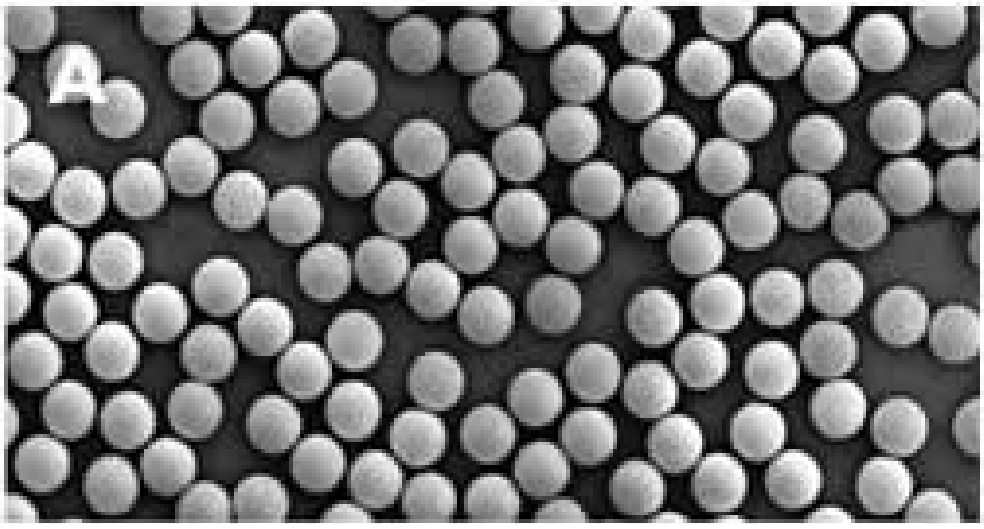

Figure 15: Photograph of the 1μm Dynabead containing SPIONs.

6.1 Low-Field NMR Relaxation Experiments [b]

Spin–lattice ^{1}H T_1 values were obtained, using a standard inversion–recovery sequence, from a Gd-DTPA-doped water sample, from a sample of magnetic beads in water, and from a sample of de-ionized water. Magnetic beads (Dynabeads MyOne Streptavidin) were purchased from Dynal Inc. The beads are 26% Fe by weight (~10% Fe by volume) with an average diameter of 1.05 ± 0.10 μm. The stock solution has a stated bead concentration of between 7×10^3 and 1.2×10^4 beads per nL (equivalent to ~2.6 mg Fe/ml). NMR samples were prepared by diluting the same batch of stock solution with de-ionized water by factors of 10, 100, and 1000 to produce nominal concentrations of 1000, 100, and 10 beads per nL. T_2^* was determined by collecting a single free-induction decay (FID) and fitting the resulting spectrum with a Lorentzian, unless noted otherwise. The relative shift of the NMR frequency of water caused by the magnetic beads was determined by measuring the resonance frequency of each solution in a 5 mm NMR tube in a conventional coil relative to a separate tube of deionized water. To avoid errors due to field drift of the permanent magnet, each frequency shift measurement was performed by switching several times between the bead solution and a deionized water sample during a period when the frequency drift was confirmed to be <1 Hz/min. All these SPION relaxation experiments were performed on the solenoid μ-coil described in Section 3.

6.2 SPION Induced Relaxation

To test the ability of the NMR μ-coils to measure spin–lattice relaxation times, we used three different water samples; the first was doped with Gd-DTPA to shorten the T_1 to around 70 ms, the second consisted of pure de-ionized water, and the third contained

the magnetic beads (at a concentration of 1000 beads/nL) in de-ionized water. In all cases, a single scan was acquired at each recovery time. Our results (**Figure 16**) show that we can accurately measure relaxation times for both shorter (65 ms) and longer (0.6 and 1.0 s) T_1 values with a standard inversion–recovery pulse sequence. The 397 μs π-pulse gave clean inversion of the magnetization for all samples.

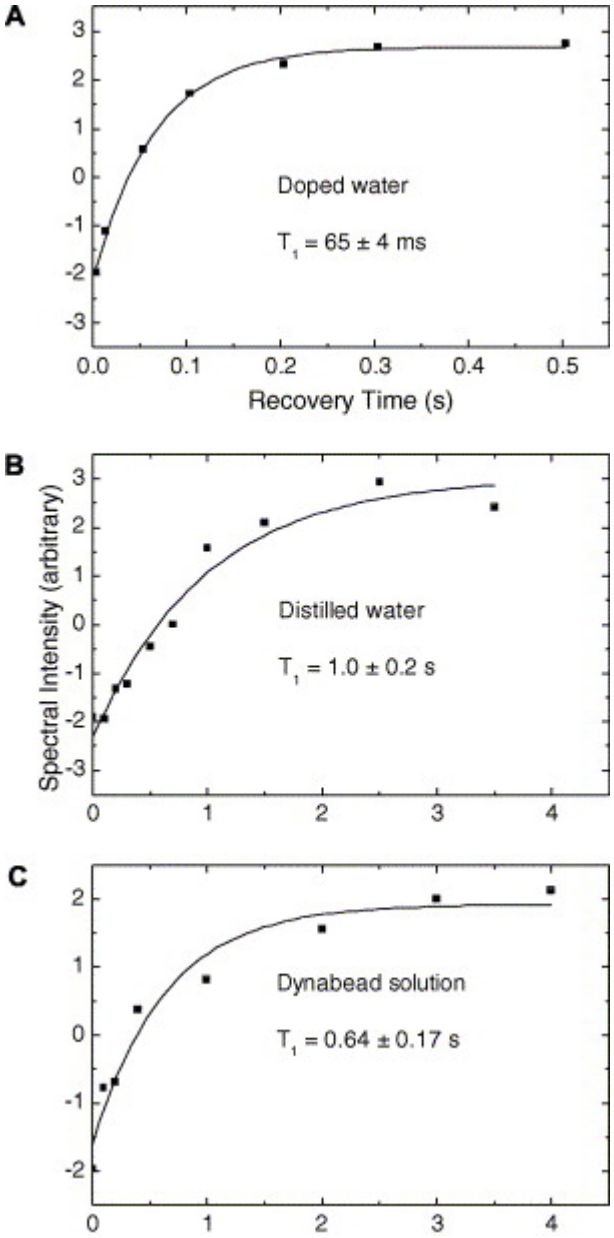

Figure 16: Measurement of the NMR spin-lattice T_1 relaxation time in solenoid 550/400 μ-coil.

In **Figure 17** is a comparison of the signal detected from DI water and three different dilutions of the stock Dynabead solution, corresponding to 1000, 100, and 10 beads/nL. The magnitude of each FID is shown so that they all appear as if they were on resonance. The data are acquired after a single π/2 pulse, digitizing at 100 μs per point (200 μs per point for the deionized water). The data were digitally filtered to achieve an effective digitization time of 400 μs per point. For the 1000 beads/nL sample, 16 FIDs were averaged together; the other data are each a single FID. The beads have two effects on the water spectral peak: the peak broadens and shifts to lower frequencies as the concentration of beads increases. The reduction in T_2^* is apparent in the FIDs. The inset compares the spectra of the four solutions and shows both the line broadening and the shift to lower frequency caused by the beads. Data for a 1 bead/nL sample (not shown) were indistinguishable from the DI water data.

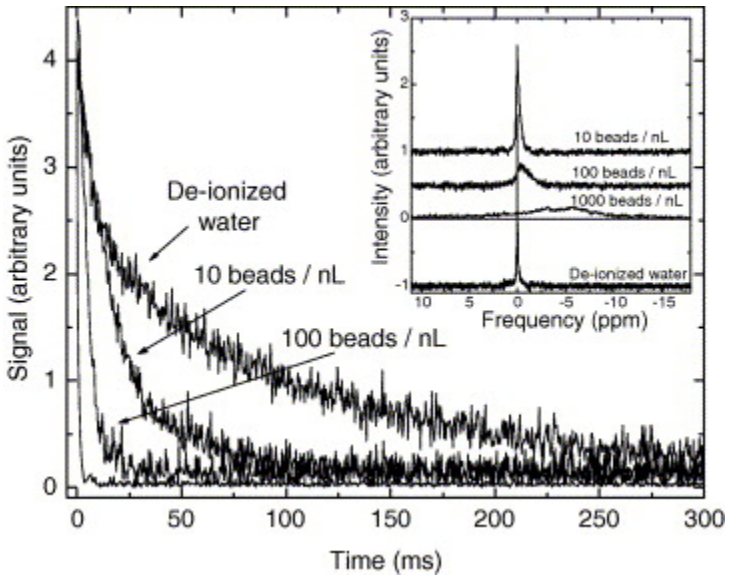

Figure 17: The ^{1}H NMR spectra for different Dynabead concentrations.

The shift of the water resonance to lower frequency in the presence of the paramagnetic beads is not surprising when one considers the line shape of water in a spherical shell of radius r surrounding a magnetized bead. The line shape is a uniaxial powder pattern (like that of the chemical shift anisotropy) due to the $3\cos^2\theta - 1$ dependence of the *z*-component of the dipolar field. The most prominent feature of this line shape is a cusp at lower frequency, corresponding to spins at $\theta \approx 90$, where the *z*-component of the bead's magnetic field is negative. Integrating this line shape over all *r* (from r_{min}, at the surface of the bead, to r_{max}, the average distance between beads) results in an approximately Lorentzian line shape.

The solid symbols in **Figure 18A** give the observed change in $1/T_2^*$ (ΔR_2^*) due to the presence of the beads, as a function of bead concentration, *C*. Here, $\Delta R_2^* = \Delta R_{2\,\text{bead solution}}^* - \Delta R_{2\,\text{water}}^*$, and $R_2^* = \pi\Delta f$, where Δf is the FWHM in Hz of the Lorentzian line fit to each spectrum in Figure 17. Note that both axes in **Figure 18A** are logarithmic; the straight line (drawn as a guide to the eye) has a slope of roughly 2/3, indicating that $\Delta R_2^* \propto C^{2/3}$ over this range of concentrations. The relaxivity $r_2^* (= \Delta R_2^* / C)$ is therefore not a constant (as defined in Eqn. 2.4), but decreases with increasing concentration as shown in **Figure 18B**.

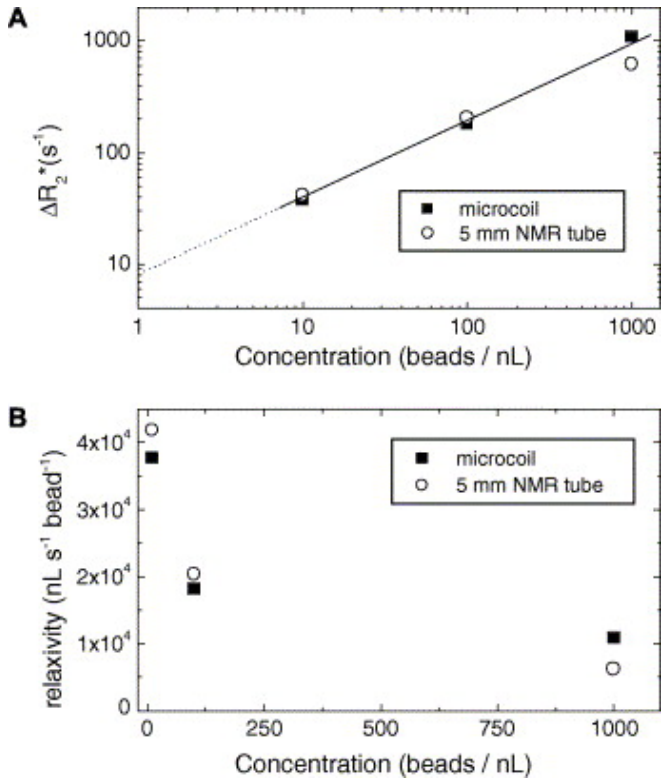

Figure 18: (A) Change in R_2 relaxation with increasing magnetic bead concentration, and (B) the relaxivity r_2 as a function of concentration.

Because magnetic field gradients can cause motion of the magnetic beads with respect to the fluid, it was not clear a priori that the concentration of beads delivered to the microcoil would be the same as the concentration in the supply syringe. Indeed, the measured T_2^* of bead solutions in the microcoil was observed to decrease over time if the bead solution was allowed to sit motionless in the coil over several minutes, suggesting that the spatial distribution of the beads was changing, due to clustering, settling, or migration out of the coil. Thus, in order to validate the microcoil results, we measured the T_2^* of the same bead solutions (1000, 100, and 10 beads/nL) and DI water in capped 5 mm NMR tubes using a conventional probe in the same magnet. Each measurement was

performed within 20–30 s after shaking the tube to homogenize the bead solution, and the tube was immediately extracted afterwards to visually confirm that the beads had not settled during the measurement. (Shimming was performed on the DI water, and a sample holder was used to position the other 5 mm tubes identically, to avoid the need to re-shim. Repeatedly placing the same sample in the probe using this holder gave line widths that were reproducible to ±5 Hz.) Migration of the beads was similarly observed in the 5 mm tubes (both visually and as an increase in T_2^* over time) if the samples were allowed to sit in the magnet for longer time periods. The ΔR_2^* values measured for the bead solutions in 5 mm tubes (open symbols in Figure 18A) are in good agreement with those obtained for the same concentrations in the microcoil, indicating that the expected concentrations were delivered to the microcoil.

6.3 Impact on SPION Amplification for Bioagent Detection

The rapid expansion of biomedical applications for magnetic nanoparticles motivates a concomitant development of the means for detecting small numbers of these intriguing agents. The most challenging goal is the detection of a single cell or molecule labeled with one magnetic bead. As discussed above, MR imaging studies [5] indicate that one bead can measurably influence the water signal in a region of length scale 100 μm surrounding the bead. Hence an NMR microcoil of diameter and length of this size (i.e., a sample volume of ~1 nL) should be optimal for detecting a single magnetic bead in an in vitro sample. A coil of this size opens up the possibility of a readily portable NMR system based on a small permanent magnet, as long as the challenges of operating a microcoil at low frequencies can be met. The line widths for de-ionized water are adequate for the detection of magnetic beads in water at a concentration of 10 beads/nL.

This inherent line width should be improved by going to smaller magnet gap sizes, for which the field homogeneity is more uniform. Our first results indicate that this approach will allow the detection of very dilute biological species, perhaps as rare as a single cell or molecule labeled with a single magnetic bead.

The challenge of achieving this detection sensitivity can be discussed quantitatively in light of the data of **Figures 17** and **18**. We envision that in a portable system, a fluid containing very dilute, magnetically labeled biological objects flows through a ~1 nL coil while the FID is monitored. The challenge is to detect the difference between the FID of the background fluid and the same fluid containing one magnetic bead within the coil volume. Considering Figure 17, we see that we can readily detect the change in T_2^* of water due to 10 beads/nL, or roughly 3000 magnetic beads in our current prototype microcoil (264 nL volume). If we can achieve a similar T_2^* for DI water ($\sim$ 100 ms) and adequate SNR in a coil with a 1 nL sample volume, we should easily be able to detect 10 beads. Extrapolating the straight line in **Figure 18A** suggests that the ΔR_2^* of one bead in a 1 nL volume is ~8 s^{-1}, which would have caused an increase in the line width of water in our current microcoil from ~3 to ~6 Hz. This increase should have been detectable given our high SNR. The fact that we did not detect a change in line width due to the 1 bead/nL solution suggests that the ΔR_2^* for this concentration is lower than that predicted by extrapolating the straight line in Figure 18A. A theoretical treatment of dipolar broadening of the NMR line due to dilute magnetic impurities indicates that the line width will be proportional to $C^{1/2}$ at higher concentrations and will be linear in C at lower concentrations. Our slope of 2/3 suggests that we are in the transition region between these two limits, and we should expect a higher slope at lower concentration,

resulting in a predicted value of ΔR_2^* lower than 8 s^{-1} at 1 bead/nL. Hence, the detection of a single 1-μm Dynabead in a 1 nL coil will require that we achieve an even narrower line width, while at the same time detecting adequate signal strength.

A 100 μm diameter coil (1 nL) will give substantially less signal than our 264 nL coil due to the reduced sample size. Thus we must consider whether such a coil will have sufficient SNR to detect 10 beads in its 1 nL volume. In the "large" microcoil data in Figure 17, we can maximize our detection sensitivity by integrating the FIDs, say from 50 to 300 ms, which is roughly equivalent to applying strong digital filtering. These integral values are 397 and 122 (arbitrary units), for the water and 10 beads/nL data, respectively. The uncertainty in these values is 3, which corresponds to a signal to noise ratio (SNR) of 133 for determining the amplitude of the water signal. The smaller 1 nL volume coil will have much less signal, but also less noise (due to its lower resistance). For microcoils in the limit where skin depth is small compared to wire size (which is not quite true for our solenoid coil), the SNR per unit volume scales as the inverse of the coil diameter (see section 4.1.5). Hence, the absolute SNR scales as the square of the linear dimension of the sample. We are proposing to scale the sample and coil dimension down by roughly a factor of 6, so we expect that the SNR in the determination of the integrated water signal amplitude will be about 3.7. Hence, the 1 nL coil will require that the beads change the area under the FID of the background water by at least 25%. Here, a concentration of 10 bead/nL caused a 70% change in the integrated signal from 50 to 300 ms, and is therefore expected to remain detectable in the 1 nL coil, assuming we achieve a similar background water T_2^*.

While our current prototype solenoid μ-coil is already capable of detecting the presence of as few as 3000 magnetic beads, it has not been optimized for maximal SNR performance for operation at 44.2 MHz. The thickness of the coil "wire" is much less than a skin depth, which raises the resistance of the coil without providing any improvements in signal detection. The width of the "wire" is much more than a skin depth, so that it may be possible to increase the number of turns per unit length and gain in coil sensitivity without suffering a nullifying increase in resistance. Careful attention to the geometrical design of our next, smaller coil, should improve the SNR above the estimate of ~3.7 based on this first attempt. SNR performance will be enhanced by reducing the coil resistance, which is higher than expected in our first ion-milled coil. Many of these issues are eliminated using the planar spiral coils described in Section 4. Improving the line width of the background fluid places a lower demand on the SNR performance. The use of susceptibility matching (either in the choice of evaporated metals or via a matching fluid) and the reduction of the filling factor (by increasing the relative wall thickness in the capillary tube) are known to improve the line widths in small coils [41]. In addition, the magnet we have used is not very homogeneous and only first order shims are available; a more homogeneous applied field may be required to achieve narrower lines. Future work in optimizing the coil will also include comparisons of both the SNR and line width performance of ion-milled coils to other types of μ-coils. We anticipate that some compromise between line width and sensitivity will provide the best opportunity for detecting single biological objects.

The surface of a single cancer cell (~10 μm in diameter) can bear upwards of 10^5 binding sites (antigens) for a particular antibody and can accommodate up to 400 1-μm

diameter magnetic beads, assuming monolayer coverage and random close packing. Thus we believe that sensitivity to 10 beads would already be adequate to detect single magnetically labeled cells. On the other hand, bacterial toxin molecules (e.g., botulism toxin) are much smaller and would accommodate only one or a few beads, requiring single-bead detection sensitivity. Hence, single-bead sensitivity remains our ultimate goal. So far, our discussion of detection limits has been based on measurements of a particular type (Dynabeads) and size (1 μm) of magnetic bead. Larger magnetic beads (having larger magnetic moments) are available and will allow us to increase the relaxivity of a single bead and further lower our detection limit. Shapiro et al. [5] observed a T_2^* of ~14 ms from single 1.63 μm diameter Bangs microbeads in 1 nL image voxels. Assuming that their background T_2^* was at least 100 ms, we calculate ΔR_2^* for a single 1.63 μm bead in a 1 nL volume to be at least 60 s^{-1}, which should be readily detected using a 1 nL microcoil with a background water T_2^* of 100 ms and a SNR of ~3. Even larger beads (e.g., 2.8-μm and 4.8-μm Dynabeads) are commercially available, and may be used, if necessary, to further enhance our ability to detect a single magnetic bead in an NMR microcoil.

7. Portable MAGRITEK NMR Instrument

The last portion of this LDRD project involved the construction of a μ-NMR system here at Sandia National Laboratories. All of the μ-coil NMR experiments described in this report were performed using the console system based at New Mexico Resonance (Albuquerque, NM). The ultimate goal was to construct a highly portable μ-NMR system that can be directly controlled by a laptop computer either locally or via remote wireless connections. To address this goal we have obtained a RF console system from MAGRITEK (New Zealand) which provides the required components and can be computer controlled via a USB connection. The NMR console system and associated laptop computer are shown in **Figure 19**. This would still be considered a research device in that it is highly flexible, and allows a range of different RF frequencies and power amplification to be controlled. Future miniaturization of this console is easily envisioned given the micro- to milli-Watt RF power range employed in the μ-coil NMR experiments described in sections 4 and 5. This MAGRITEK console is run using the PROSPA software package (display shown in **Figure 19**) and is highly flexible allowing the individual users to create macros specific for their desired application.

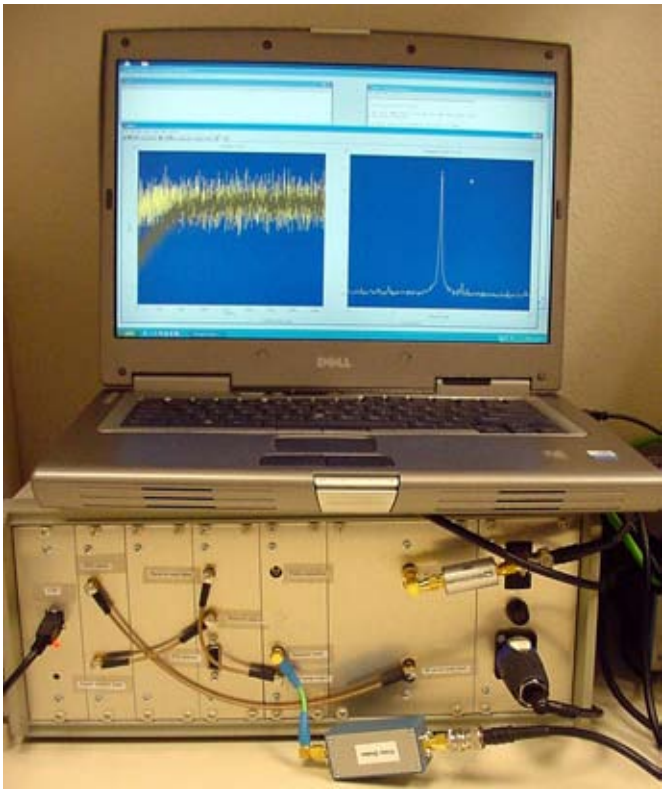

Figure 19: MAGRITEK NMR system.

We have also completed the construction and initial testing of a 40 MHz NMR probe (shown in **Figures 20 and 21**) to be used with this MAGRITEK console on the 0.96 Tesla magnet presently housed at Sandia. The 40 MHz tuning circuit is presented in Appendix 4. The positioning of the μ-coils within the permanent magnetic field is known to be very crucial, such that we have designed a coupling between this μ-probe and a 3-way micro-positioner for fine control of the NMR probes location. This system is presently being further developed and tested, and will be delivered to the Department of Biochemistry and Molecular Biology, University of New Mexico as a part of a current WRCE (Western Regional Center of Excellence) for Biodefense projects.

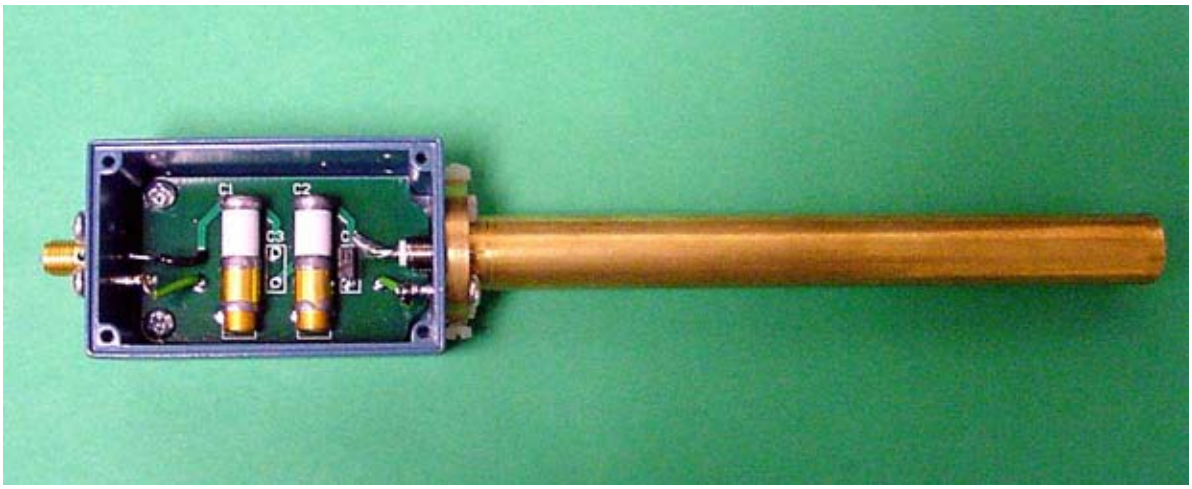

Figure 20: 40 MHz μ-NMR probe.

Figure 21: 40 MHz μ-NMR probe with 3-way micro-positioner

8. Conclusions

We have demonstrated that it is possible to detect the amplification of water relaxation induced by the presence of SPIONs in solution using a μ-NMR device. These results show that concentrations as low as 10 SPION particles per nL can be detected based on NMR relaxation experiments. This LDRD provides a "proof of principle" for the ability of μ-NMR to be used to detect bio-agents through nanoparticle amplification at very low concentrations. To optimize the detection limit, two individual NMR μ-coil

platforms that have detection volumes on the order of 250 nL were fabricated and tested. These initial μ-NMR experiments have allowed the down-selection of the planar spiral μ-coil platform as the design that will be pursued for future μ-NMR development. We have also demonstrated that a novel tuning circuit, capable of tuning an arbitrarily small inductance at a frequency compatible with a permanent magnet, coupled with a microcoil, allows spectroscopic and relaxation measurements using less than 1 mW of radiofrequency power. (This low power requirement further aids in making the NMR system portable.)

Micro-NMR provides a robust, portable device that allows analysis of solution streams that are not optically transparent (blood, effluent etc.), and thus provides an alternative μ-scale detection platform to other detection systems. Future development directions that we will pursue for this μ-NMR device include the coupling of other μ-fluid components to this detection platform, along with the miniaturization of the permanent magnet system.

9. References

[1]. Bjornerud, A.; Johansson, L., The Utility of Superparamagnetic Contrast Agents in MRI: Theoretical Consideration and Applications in the Cardiovascular System. *NMR in Biomedicine* **2004,** 17, 465-477.

[2]. Winter, P. M.; Caruthers, S. D.; Kassner, A.; Harris, T. D.; Chinen, L. K.; Allen, J. S.; Lacy, E. K.; Zhang, H.; David, R. J.; Wickline, S. A.; Lanza, G. M., Molecular Imaging of Angiogenesis in Nascent Vx-2 Rabbit Tumors Using a Novel avB3-targeted Nanoparticle and 1.5 Tesla Magnetic Resonance Imaging. *Cancer Research* **2003,** 63, 5838-5843.

[3]. Jun, Y.-w.; Huh, Y.-M.; Choi, J.-s.; Lee, J.-H.; Song, H.-T.; Kim, S.; Yoon, S.; Kim, K.-S.; Shin, J.-S.; Suh, J.-S.; Cheon, J., Nanoscale Size Effects of Magnetic Nanocrystals and Their Utilization for Cancer Diagnostics via Magnetic Resonance Imaging. *J. Am. Chem. Soc.* **2005,** 127, 5732-5733.

[4]. Perez, J. M.; Simeone, F. J.; Saeki, Y.; Josephson, L.; Weissleder, R., Viral-Induced Self Assembly of Magnetic nanoparticles Allows the Detection of Viral Particles in Biological Media. *J. Am. Chem. Soc.* **2003,** 125, 10192-10193.

[5]. Shapiro, E. M.; Skrtic, S.; Sharer, K.; Hill, J. M.; Dunbar, C. E.; Koretsky, A. P., MRI Detection of Single Particles for Cellular Imaging. *Proceedings National Academy of Science* **2004,** 101, (30), 10901-10906.

[6]. Zhao, X.; Hillard, L. R.; Mechery, S. J.; Wang, Y.; Bagwe, R. P.; Jin, S.; Tan, W., A Rapid Bioassay for Single Bacterial Cell Quantitation Using Bioconjugated Nanoparticles. *Proceedings National Academy of Science* **2004,** 101, (42), 15027-15032.

[7]. Artemov, D., Molecular Magnetic Resonance Imaging With Targeted Contrast Agents. *Journal of Cellular Biochemistry* **2003,** 90, (3), 518-524.

[8]. Artemov, D.; Mori, N.; Okollie, B.; Bhujwalla, Z. M., MR Molecular Imaging of the Her-2/neu Receptor in Breast Cancer Cells Using Targeted Iron Oxide Nanoparticles. *Magnetic Resonance in Medicine* **2003,** 49, (3), 403-8.

[9]. Artemov, D.; Mori, N.; Ravi, R.; Bhujwalla, Z. M., Magnetic Resonance Molecular Imaging of the HER-2/neu Receptor. *Cancer Research* **2003,** 63, (11), 2723-2727.

[10]. Artemov, D.; Ravi, R.; Okollie, B.; Bhujwalla, Z. M., MR Molecular Imaging of HER-2/neu Receptor with Targeted Contrast Agents. *Proceedings of the American Association for Cancer Research Annual Meeting*

94th Annual Meeting of the American Association for Cancer Research; July 11-14, 2003; Washington, DC, USA **2003,** 44, 692-693.

[11]. Perez, J. M.; O'Loughin, t.; Simeone, F. J.; Weissleder, R.; Josephson, L., DNA-Based Magnetic Nanoparticle Assembly Acts as a Relaxation Nano-Switch Allowing Screening of DNA-Cleaving Agents. *J. Am. Chem. Soc.* **2002,** 124, (12), 2856-2857.

[12]. Frias, J. C.; Williams, K. J.; Fisher, E. A.; Fayad, Z. A., Recombinant HDL-Like Nanoparticles: A Specific Contrast Agent for MRI of Atherosclerotic Plaques. *J. Am. Chem. Soc.* **2004,** 126, 16316-16317.

[13]. Roch, A.; Gossuin, Y.; Muller, R. N.; Gillis, P., Superparamagnetic Colloidal Suspensions: Water Magnetic Relaxation and Clustering. *J. Magnetism Magnetic Materials* **2005,** 293, 532-539.

[14]. Roch, A.; Muller, R. N.; Gillis, P., Theory of Proton Relaxation Induced by Superparamagnetic Particles. *J. Chem. Physics* **1999,** 110, (11), 5403-5411.

[15]. Lacey, M. E.; Subramanian, R.; Olson, D. L.; Webb, A. G.; Sweedler, J. V., High-Resolution NMR Spectroscopy of Sample Volumes from 1 nl to 10 µl. *Chem. Rev.* **1999,** 99, 3133-3152.

[16]. Minard, K. R.; Wind, R. a., Solenoid Microcoil Design. Part I: Optimizing RF Homogeneity. *Concepts in Magnetic Resonance* **2001,** 13, (2), 128-142.

[17]. Minard, K. R.; Wind, r. A., Solenoidal Microcoil Design - Part II: Optimizing Winding Parameters for Maximum Signal-to-Noise Performance. *Concepts in Magnetic Resonance* **2001,** 13, (3), 190-210.

[18]. Sorli, B.; Chateaux, J. F.; Pitival, M.; Chahboune, H.; Favre, B.; Briguet, A.; Morin, P., Micro-spectrometer for NMR: Analysis of small Quantities in Vitro. *Meas. Sci. Technol.* **2004,** 15, 877-880.

[19]. Trumbull, J. D.; Glasgow, I. K.; Beebe, D. J.; Magin, R. L., Integrating Microfabricated Fluidic Systems and NMR Spectroscopy. *IEEE Transactions on Biomedical Engineering* **2000,** 47, (1), 3-7.

[20]. Walton, J. H.; de Roop, J. S.; Shutov, M. V.; Goloshevky, A. G.; McCarthy, M. J.; Smith, R. L.; Collins, S. D., A Micromachined Double-Tuned NMR Microprobe. *Anal. Chem.* **2003,** 75, 5030-5036.

[21]. Dechow, J.; Forchel, A.; Lanz, T.; Haase, A., Fabrication of NMR - Microsensors for Nanoliter Sample Volumes. *Micoelectronic Engineering* **2000,** 53, 517-519.

[22]. Eroglu, S.; Gimi, B.; Roman, B.; Friedman, G.; Magin, R. L., NMR Spiral Surface Microcoils: Design, Fabrication and Imaging. *Concepts in Magnetic Resonance* **2003,** 17B, 1-10.

[23]. Massin, C.; Boero, G.; Vincent, F.; Abenhaim, J.; Besse, P.-A.; Popovic, R. S., High-Q Factor RF Planar Microcoils for Micro-Scale NMR Spectroscopy. *Sensors and Actuators A* **2002,** 97-98, 280-288.

[24]. Massin, C.; Vincent, F.; Homsy, A.; Ehrmann, K.; Boero, G.; Besse, P.-A.; Daridon, A.; Verpoorte, E.; de Rooij, N. F.; Popovic, R. S., Planar Microcoil-Based Microfluidic NMR Probes. *J. Magn. Res.* **2003,** 164, 242-255.

[25]. Rogers, J. A.; Jackman, R. J.; Whitesides, G. M.; Olson, D. L.; Sweedler, J. V., Using Microcontact Printing to Fabricate Microcoils on Capillaries for High resolution Proton Nuclear Magnetic Resonance on Nanoliter Volumes. *Appl. Phys. Lett.* **1997,** 70, (18), 2464-2466.

[26]. Malba, V.; Maxwell, R.; Evans, L. B.; Bernhardt, A. F.; Cosman, M.; Yan, k., Laser-Lathe Lithography - a Novel Method for Manufacturing Nuclear Magnetic Resonance Microcoils. *Biomedical Microdevices* **2003,** 5, (1), 21-27.

[27]. Wolters, A. M.; Jayawickrama, D. A.; Larvie, C. K.; Sweedler, J. V., Capillary Isotachophoresis/NMR: Extension to Trace Impurity Analysis and Improved Instrument Coupling. *Anal. Chem.* **2002,** 74, 2306-2313.

[28]. Wolters, A. M.; Jayawickrama, D. A.; Sweedler, J. V., Microscale NMR. *Current Opinions in Chemical Biology* **2002,** 6, 711-716.

[29]. Wolters, A. M.; Jayawickrama, D. A.; Webb, A. G.; Sweedler, J. V., NMR Detection with Multiple Solenoid Microcoils for Continuous-Flow Cappillary Electrophoresis. *Anal. Chem.* **2002,** 74, 5550-5555.

[30]. Berry, L.; Renaud, L.; Kleimann, P.; Morin, P.; Armenean, M.; Saint-Jalmes, H., Development of Implantable Detection Microcoils for Minimally Invasive NMR Spectroscopy. *Sensors and Actuators A* **2001,** 93, 214-218.

[31]. Renaud, L.; Armenean, M.; Berry, L.; Kleimann, P.; Morin, P.; Pitival, M.; O'Brien, J.; Brunet, M.; Saint-Jalmes, H., Implantable Planar RF Microcoils for NMR Microspectroscopy. *Sensors and Actuators A* **2002,** 99, 244-248.

[32]. Syms, R. R. A.; Ahmad, M. M.; Young, I. R.; Li, Y.; Hand, J.; Gilderdale, D., MEMS Helmholtz Coils for Magnetic Resonance Imaging. *J. Micromechanics and Microengineering* **15,** 15, S1-S9.

[33]. Goloshevky, A. G.; Walton, J. H.; Shutov, M. V.; de Ropp, J. S.; Collins, S. D.; McCarthy, M. J., Nuclear Magnetic Resonance Imaging for Viscosity Measurements of Non-Newtonian Fluids Using a Miniaturized RF Coil. *Measurement Science and Technology* **2005,** 16, 513-518.

[34]. Goloshevky, A. G.; Walton, J. H.; Shutov, M. V.; De Roop, J. S.; Collins, S. D.; McCarthy, M. J., Integration of Biaxial Planar Gradient Coils and an RF Microcoil for NMR Flow Imaging. *Meas. Sci. Technol.* **2005,** 16, 505-512.

[35]. Seeber, D. A.; Cooper, R. L.; Ciobanu, L.; Pennington, C. H., Design and testing of High Sensitivity Microreciever Coil Apparatus for Nuclear Magnetic Resonance and Imaging. *Review of Scientific Instruments* **2001,** 72, (4), 2171-2179.

[36]. Boero, G.; Frounchi, J.; Furrer, B.; Besse, P.-A.; Popovic, R. S., Fully Integrated Probe for Proton nuclear Magnetic Resonance Magnetometry. *Review of Scientific Instruments* **2001,** 72, (6), 2764-2768.

[37]. Goloshevky, A. G.; Walton, J. H.; Shutov, M. V.; De Roop, J. S.; Collins, S. D.; McCarthy, M. J., Development of Low Filed Nuclear Magnetic Resonance Microcoils. *Review of Scientific Instruments* **2005,** 76, 024101-024106.

[38]. Morales, M. P.; Bomati-Miguel, O.; Perez de Alejo, R.; Ruiz-Cabello, J.; Veintemillas-Verdaguer, S.; O'Grady, K., Contrast Agents for MRI Based on Iron Oxide Nanoparticles Prepared by Laser Pyrolysis. *J. Magnetism Magnetic Materials* **2003,** 266, 102-109.

[39]. Peck, T. L.; Magin, R. L.; Lauterbur, P. C., Design and Analysis of Microcoils for NMR Spectrosocopy. *J. Magn. Res., B.* **1995,** 108, 114-124.

[40]. Vasile, M. J.; Biddick, C.; Schwalm, S., Microfabrication by Ion Milling: The Lathe Technique. *J. Vac. Sci. Technology B* **1994,** 12, 2388.

[41]. Webb, A. G.; Grant, S. C., Signal-to-Noise and Magnetic Susceptibility Trade-offs in Solenoidal Microcoils for NMR. *J. Magn. Res., B.* **1996,** 113, 83-87.

Appendix 1. Fabrication layout of planar spiral micro-coils with electrical contact pads shown.

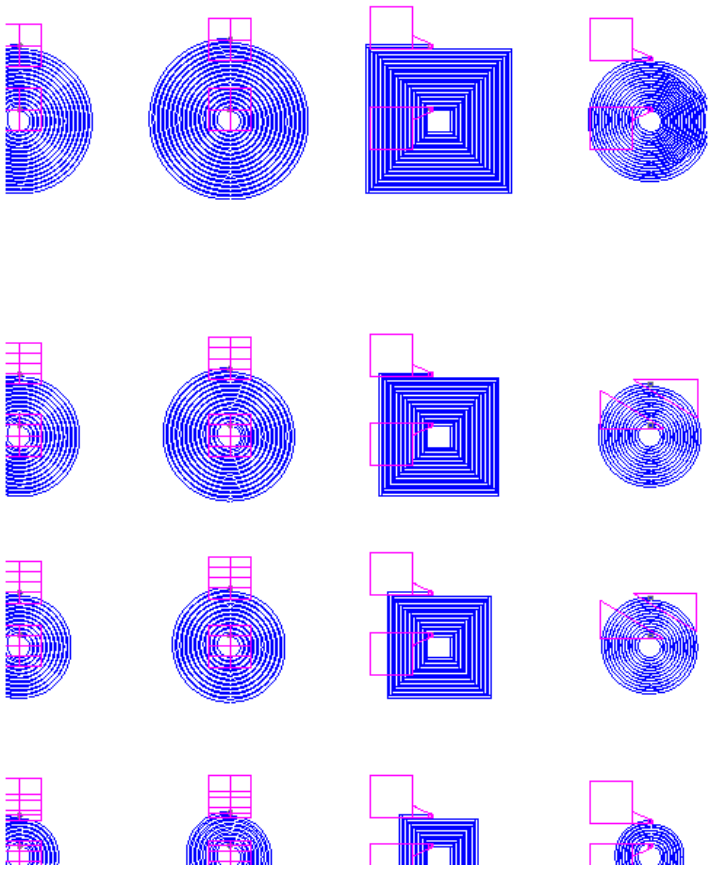

Appendix 2. MATHCAD analysis of planar micro-coils performance for different design criteria (J. D. Williams).

Physical Properties of gold

$\psi := 1930\,\frac{kg}{m^3}$ $\rho := 2.2\cdot10^{-8}\,\Omega\cdot m$ $\mu := 1.256\cdot10^{-6}\,T\cdot\frac{m}{A}$ $\mu o := 4\cdot\pi\cdot10^{-7}\cdot\frac{N}{A^2}$

$\nu := 1\cdot10^{6}\cdot Hz, 6\cdot10^{6}Hz .. 600\cdot10^{6}Hz$

$\delta(\nu) := \sqrt{\frac{2\cdot\rho}{2\cdot\pi\cdot\nu\cdot\mu}}$ Skin depth in m $\delta\left(\frac{42.47\cdot10^{6}Hz}{2\cdot\pi}\right) = 2.872\times10^{-5}\,m$

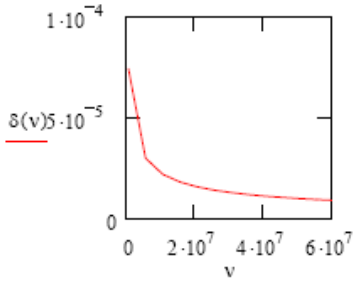

Coil Constants

line width $w := 10\cdot10^{-6}m, 11\cdot10^{-6}m .. 100\cdot10^{-6}m$

Spacing $S := 10\cdot10^{-6}m, 11\cdot10^{-6}m .. 100\cdot10^{-6}m$

Height $h := 5\cdot10^{-6}m, 6\cdot10^{-6}m .. 150\cdot10^{-6}m$

number of turns $n := 1, 2 .. 20$

Length of the Conductor

Internal radius $ri := 250\cdot10^{-6}m$

External radius $re(n,w,S) := ri + (w + S)(n - 1)$

Coil Length $l(n,w,S) := n\cdot\pi\cdot(ri + re(n,w,S) + w)$

Effective RF constants

$$weff(\nu,w) := 2\cdot\delta(\nu)\cdot\frac{\cosh\left(\frac{w}{\delta(\nu)}\right) - \cos\left(\frac{w}{\delta(\nu)}\right)}{\sinh\left(\frac{w}{\delta(\nu)}\right) + \sin\left(\frac{w}{\delta(\nu)}\right)}$$

$$heff(\nu,h) := 2\cdot\delta(\nu)\cdot\frac{\cosh\left(\frac{h}{\delta(\nu)}\right) - \cos\left(\frac{h}{\delta(\nu)}\right)}{\sinh\left(\frac{h}{\delta(\nu)}\right) + \sin\left(\frac{h}{\delta(\nu)}\right)}$$

$Seff(\nu,w,h) := w\cdot h - (w - weff(\nu,w))\cdot(h - heff(\nu,h))$

Electrical Resistance

$$Rc(n,\nu,w,S,h) := \frac{\rho \cdot l(n,w,S)}{Seff(\nu,w,h)}$$

$$RcDC(n,w,S,h) := \left(\frac{\rho}{h \cdot w}\right) \cdot \pi \cdot \left[(w + S) \cdot n^2 + 2 \cdot n \cdot \left[ri - \frac{1}{2} \cdot (S)\right]\right]$$

Magnetic Field Strength

$$B(n,w,S) := \mu o \cdot \left[\sum_{q=1}^{n} \frac{1}{2 \cdot [ri + (w + S) \cdot (q - 1)]}\right]$$

Signal to Noise Ratio

$$SNR(n,\nu,w,S,h) := \frac{B(n,w,S)}{\sqrt{Rc(n,\nu,w,S,h)}}$$

Coil Inductance

$$Const := 14 \cdot 10^{-7} \cdot \frac{H}{m}$$

$$L(n,w,S) := Const \cdot n^2 \cdot \frac{(re(n,w,S) + ri + w)^2}{2.14 \cdot re(n,w,S) - ri + 0.57 \cdot w}$$

Quality Factor

$$\omega(\nu) := 2 \cdot \pi \cdot \nu \qquad aa := \frac{42.57 \cdot 10^6 Hz}{2 \cdot \pi}$$

$$Q(n,\nu,w,S,h) := \frac{\omega(\nu) \cdot L(n,w,S)}{Rc(n,\nu,w,S,h)}$$

$$Rc\left(10, aa, 60 \cdot 10^{-6} m, 50 \cdot 10^{-6} m, 60 \cdot 10^{-6} m\right) = 0.3\,\Omega$$

Conclusions

Increases in hieght produces a linear increase in SNR, and Q: Set h=50*10^(-6) m

Frequency if fixed for spectroscopic reasons: w=42.57 MHz

Ideal field strength is 50 G: or 5 mT/A

$$SNR(n, \nu, w, S, h) := \frac{B(n, w, S)}{\sqrt{Rc(n, \nu, w, S, h)}}$$

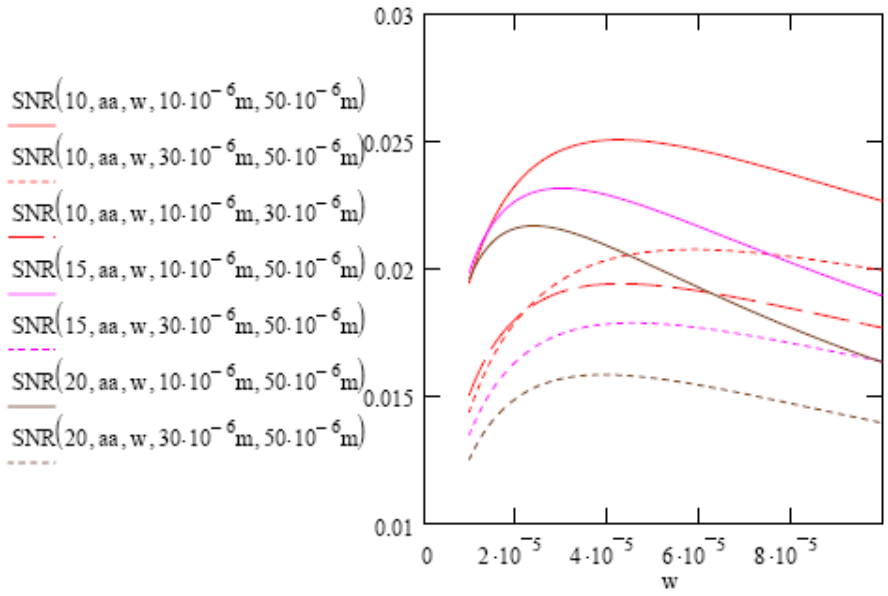

$$nSNR(n,w) := SNR\left(n, aa, w, 40\cdot10^{-6}m, 60\cdot10^{-6}m\right)$$

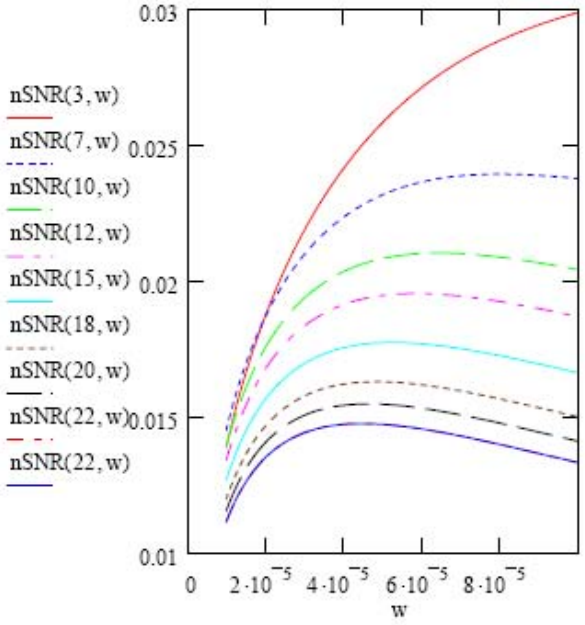

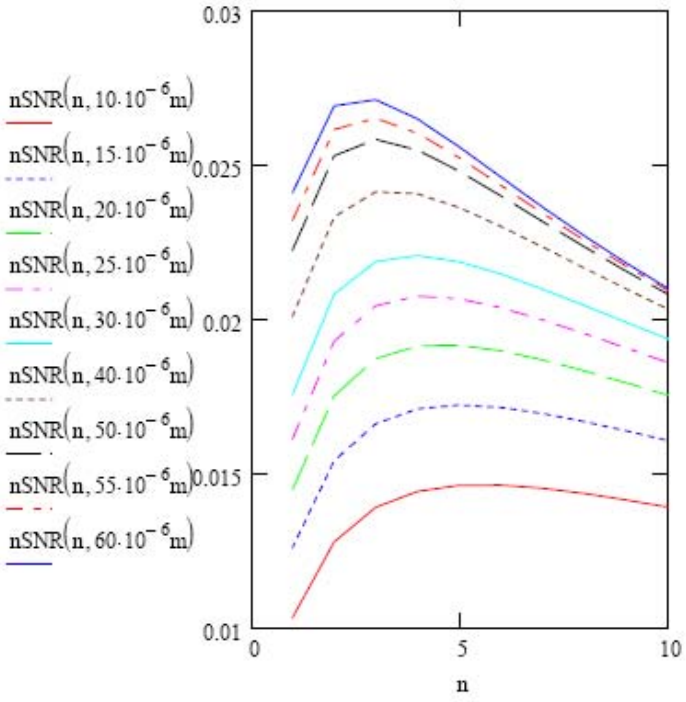

$$SSNR(S,w) := SNR\left(10, aa, w, S, 60\cdot10^{-6}m\right)$$

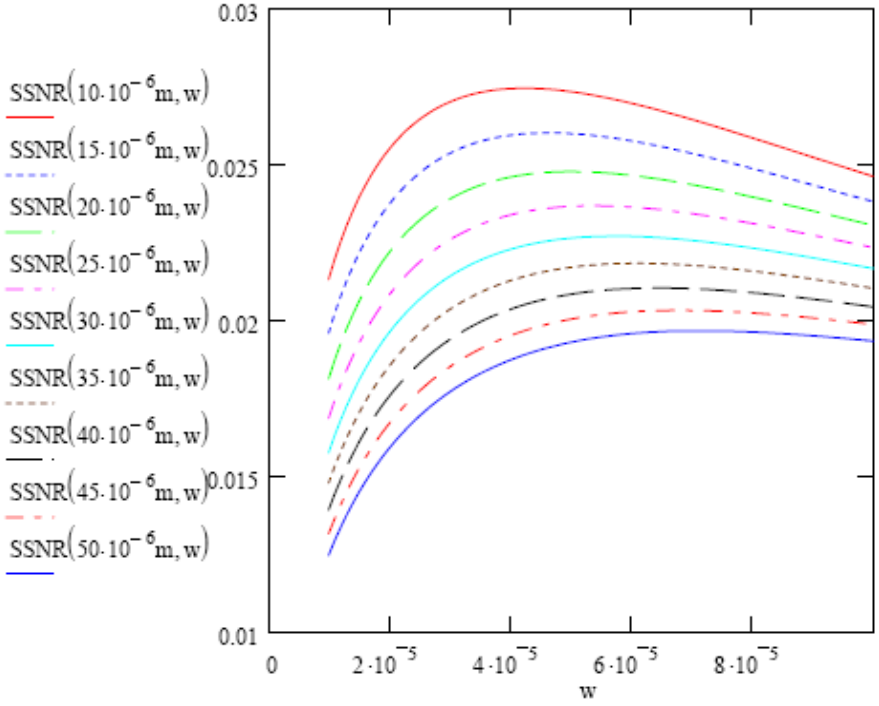

$$Q\left(10, aa, 60\cdot10^{-6}m, 40\cdot10^{-6}m, 60\cdot10^{-6}m\right) = 20.014$$

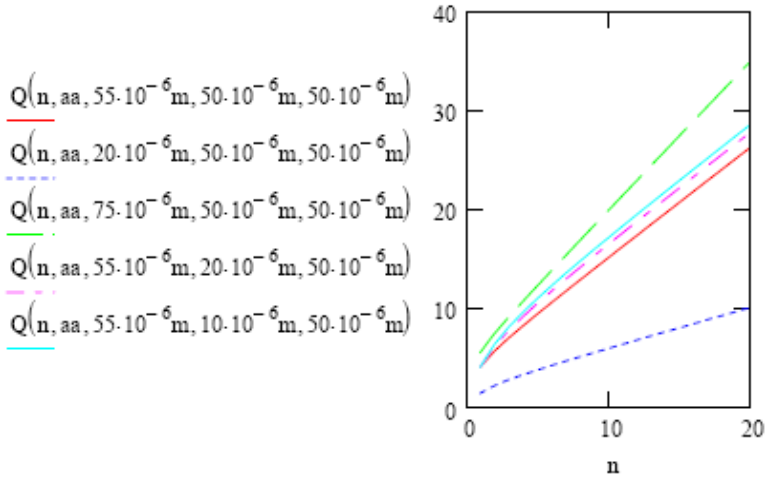

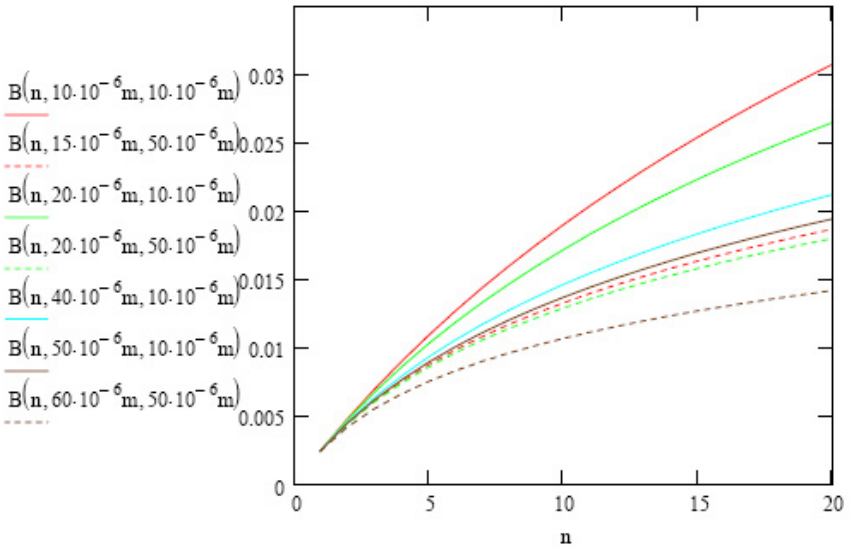
B(n, 10·10⁻⁶m, 10·10⁻⁶m)
B(n, 15·10⁻⁶m, 50·10⁻⁶m)
B(n, 20·10⁻⁶m, 10·10⁻⁶m)
B(n, 20·10⁻⁶m, 50·10⁻⁶m)
B(n, 40·10⁻⁶m, 10·10⁻⁶m)
B(n, 50·10⁻⁶m, 10·10⁻⁶m)
B(n, 60·10⁻⁶m, 50·10⁻⁶m)
0.03
0.025
0.02
0.015
0.01
0.005
0
0
5
10
15
20
n

$$z := 1\cdot10^{-6}\,m, 2\cdot10^{-6}\,m .. 300\cdot10^{-6}\,m$$

$$Bz(n,w,S,z) := \mu o\cdot\left[\sum_{q=1}^{n}\frac{1}{2\cdot[ri+(w+S)\cdot(q-1)]}\right]\cdot\frac{ri^3}{\left(ri^2+z^2\right)^{\frac{3}{2}}}$$

$$B\left(7,55\cdot10^{-6}\,m,50\cdot10^{-6}\,m\right) = 9.224\times10^{-3}\,\frac{kg}{s^2A^2}$$

$$Bz\left(7,55\cdot10^{-6}\,m,50\cdot10^{-6}\,m,150\cdot10^{-6}\,m\right) = 5.816\times10^{-3}\,\frac{kg}{s^2A^2}$$

$$B\left(10,60\cdot10^{-6}\,m,40\cdot10^{-6}\,m\right) = 0.011\,\frac{kg}{s^2A^2}$$

$$Bz\left(10,60\cdot10^{-6}\,m,40\cdot10^{-6}\,m,1\cdot10^{-6}\,m\right) = 0.011\,\frac{kg}{s^2A^2}$$

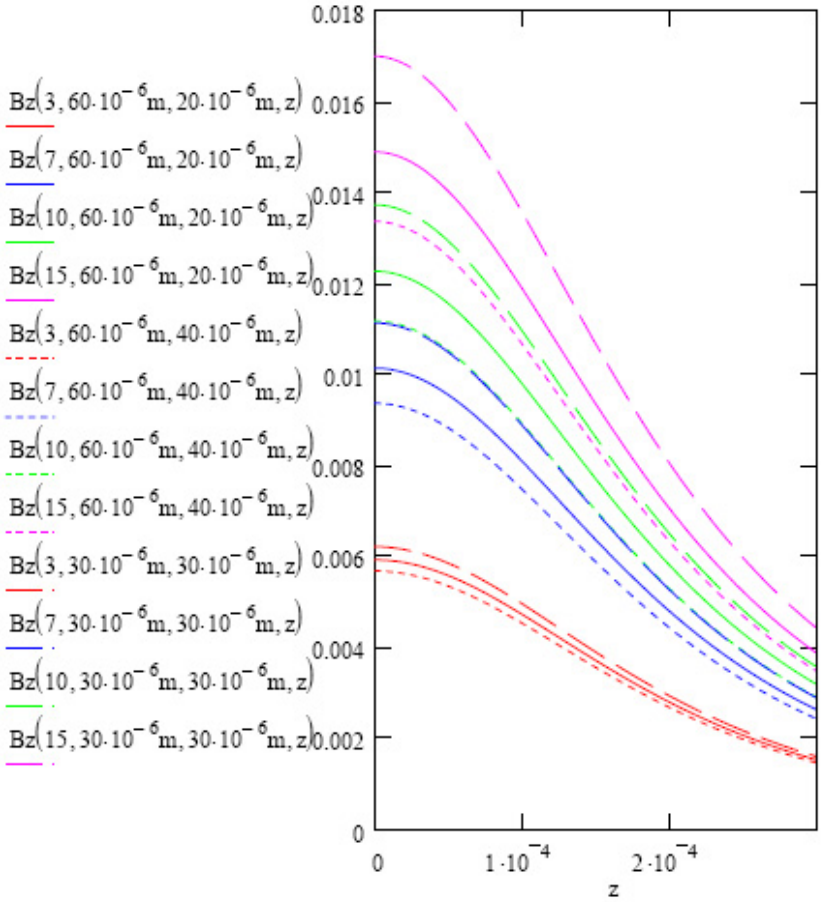

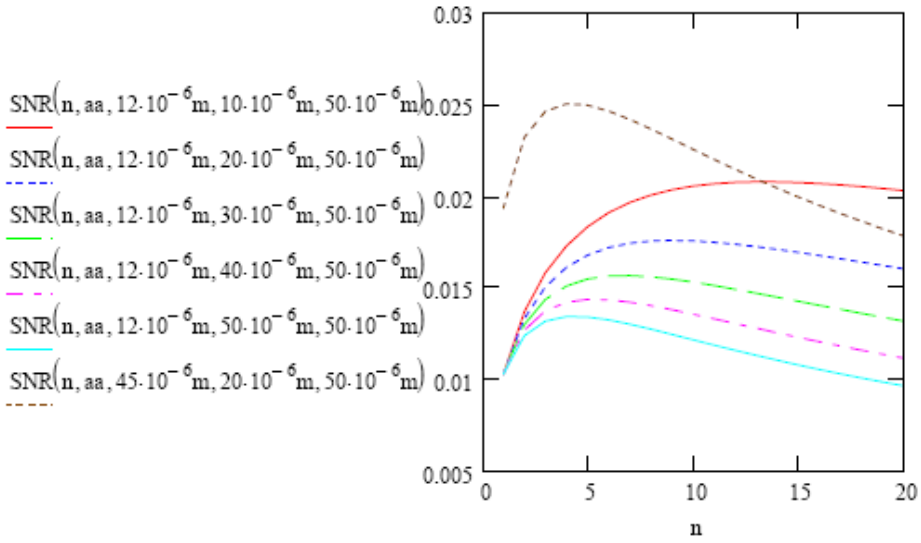
SNR(n, aa, 12·10⁻⁶m, 10·10⁻⁶m, 50·10⁻⁶m)
SNR(n, aa, 12·10⁻⁶m, 20·10⁻⁶m, 50·10⁻⁶m)
SNR(n, aa, 12·10⁻⁶m, 30·10⁻⁶m, 50·10⁻⁶m)
SNR(n, aa, 12·10⁻⁶m, 40·10⁻⁶m, 50·10⁻⁶m)
SNR(n, aa, 12·10⁻⁶m, 50·10⁻⁶m, 50·10⁻⁶m)
SNR(n, aa, 45·10⁻⁶m, 20·10⁻⁶m, 50·10⁻⁶m)
0.03
0.025
0.02
0.015
0.01
0.005
0
5
10
15
20
n

Appendix 3. DC Electrical Characterization of Microcoils
by Edna Cárdenas and Steve Howell

Electrical measurements were made on each coil using a probe station which allowed us to construct a four probe circuit connection (Figure 1). A Keithley 2700 sourced a variable DC current which was applied to a probe tip connected to one coil electrode. On the other electrode a similar probe tip completed the circuit back to the Keithley 2700. Two additional probe tips were used to measure the voltage across the coil. A Keithley 6514 electrometer recorded the voltage values. The electrometer served as a high-input impedance voltage meter, restricting the amount of current flowing through the probe tips' electrical connection. This setup minimizes the effects of the contact resistance.

The source meter was used to sweep a consecutive range of current values between -100 mA to 100 mA in 10 mA increments. From the data and using a best fit line, we obtained a value for the resistance from the slope and by using Ohm's Law.

Coils numbered five and forty were found to be damaged during optical inspection and therefore not measured. Of the remaining fifty-three coils measured, seven were found to be electrically open (13%) and labeled as damaged. Devices were determined to be an open circuit if the electrometer measured an overflow for the voltage reading, implying a break in the circuit connection through the coil.

Table 1 lists the calculated resistance values for each coil measured.

Table 1

Date Measured	Coil #	Resistance	# Coils	Geometry
4/6/2006	1	damaged	15	circular
4/6/2006	2	4.36E-02	3	circular
4/6/2006	3	damaged	7	circular
4/6/2006	4	2.89E-01	10	circular
4/6/2006	6	3.72E-01	7	circular
4/6/2006	7	damaged	12	circular
4/6/2006	8	4.97E-01	12	circular
4/6/2006	9	5.41E-02	3	circular
4/6/2006	10	2.48E-01	10	circular
4/6/2006	11	5.26E-02	3	circular
4/6/2006	12	4.87E-01	12	square
4/6/2006	13	1.11E+00	10	circular
4/6/2006	14	3.68E-01	12	circular
4/6/2006	15	3.88E-01	12	circular
4/6/2006	16	damaged	15	circular
4/6/2006	17	6.16E-01	12	circular
4/6/2006	18	damaged	--	circular
4/6/2006	19	5.03E-01	15	circular
4/6/2006	20	damaged	15	circular
4/6/2006	21	3.38E-01	12	circular
4/6/2006	22	6.53E-02	3	square

Date Measured	Coil #	Resistance	# Coils	Geometry
4/6/2006	23	damaged	12	circular
4/6/2006	24	3.91E-01	10	square
Not measured	25	----	3	circular
4/6/2006	26	3.80E-02	3	circular
4/6/2006	27	5.79E-02	3	circular
4/6/2006	28	5.26E-02	3	circular
4/6/2006	29	5.27E-02	3	circular
4/6/2006	30	4.77E-02	3	circular
Not measured	31	----	3	circular
4/6/2006	32	6.79E-02	3	square
4/6/2006	33	6.88E-02	3	square
4/6/2006	34	2.21E-01	7	square
4/6/2006	35	1.48E-01	7	circular
4/6/2006	36	1.66E-01	7	circular
4/6/2006	37	1.57E-01	7	circular
4/6/2006	38	1.40E-01	7	circular
4/6/2006	39	1.60E-01	7	circular
4/6/2006	41	1.69E-01	7	circular
4/6/2006	42	4.71E-01	12	square
Not measured	43	----	7	circular
4/6/2006	44	4.01E-01	12	circular
4/6/2006	45	6.02E-01	15	circular
4/6/2006	46	3.71E-01	12	circular
4/6/2006	47	5.51E-01	15	circular
4/6/2006	48	2.16E-01	7	square
4/6/2006	49	4.00E-01	12	circular
4/6/2006	50	1.61E-01	7	circular
4/6/2006	51	3.84E-01	12	circular
4/6/2006	52	1.64E-01	7	circular
4/6/2006	53	3.69E-01	12	circular
4/6/2006	54	3.25E-01	12	circular
4/6/2006	55	3.77E-01	12	circular
4/6/2006	56	1.34E-02	12	circular
4/6/2006	57	5.03E-01	12	circular

Figure 2

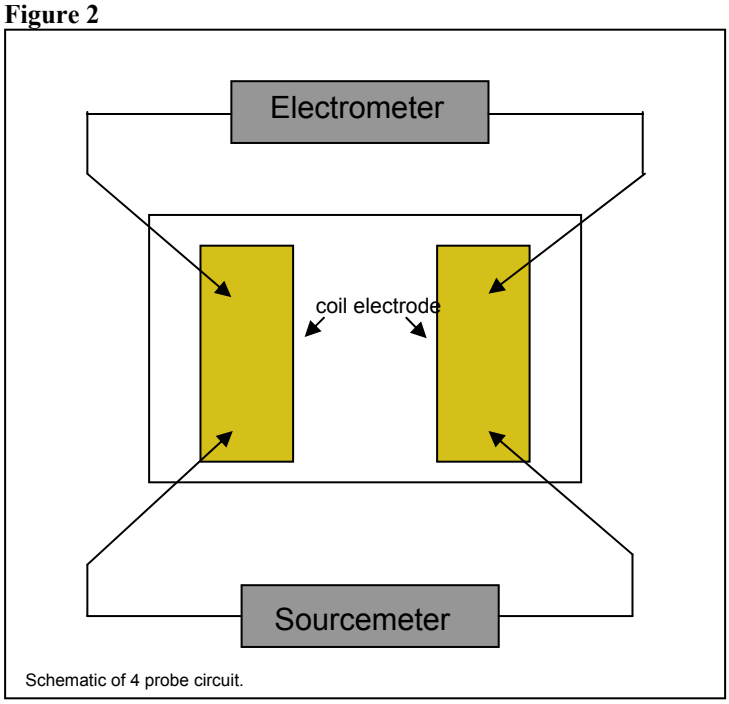

Schematic of 4 probe circuit.

Appendix 4. Circuit layout and printed circuit board layout for 40 MHz tuning and detection circuit.

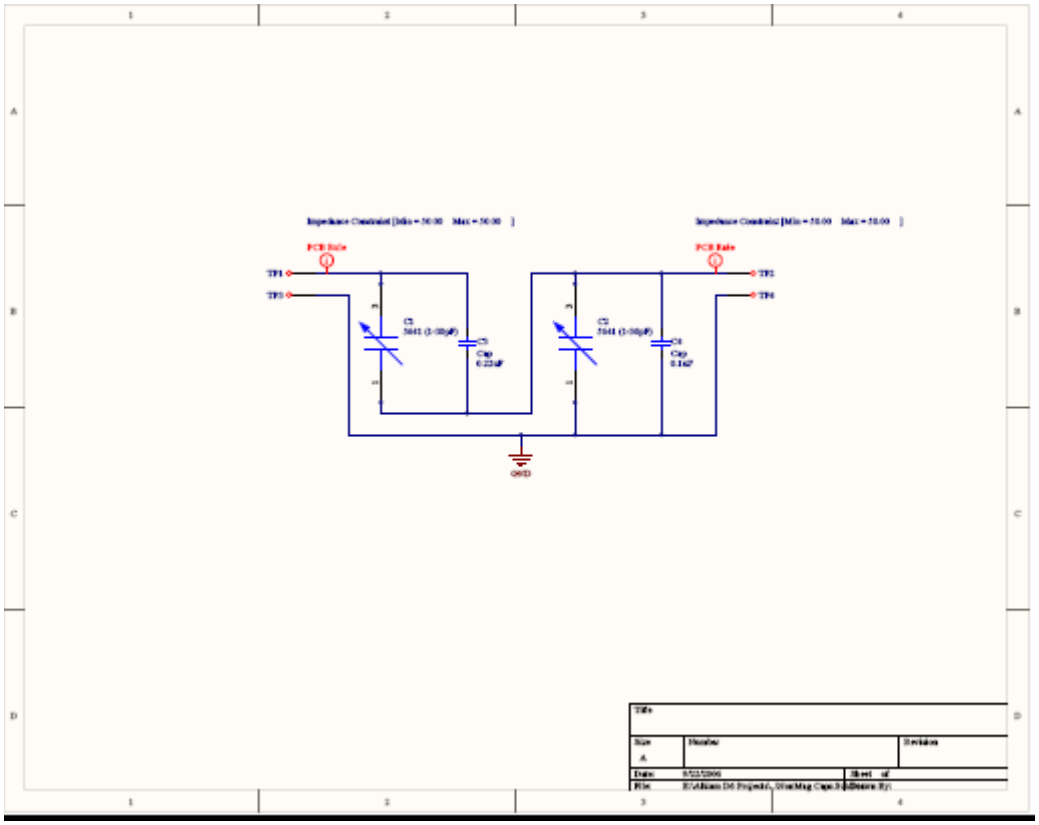

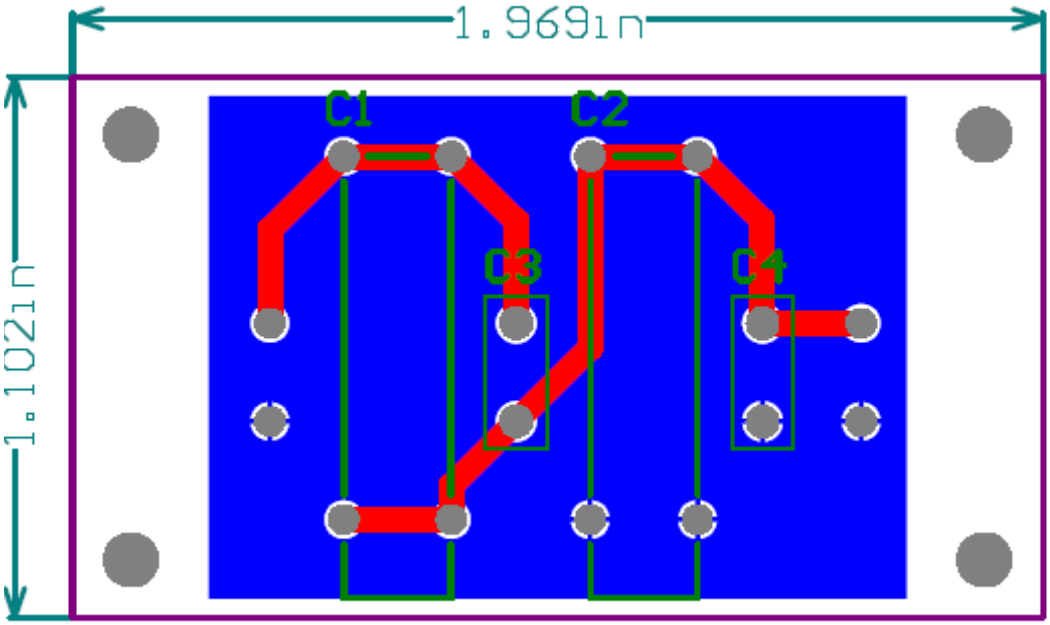
1.969in
1.102in
C1
C2
C3
C4

Distribution

10	MS0886	Todd M. Alam, 1816
1	MS 0885	Justine Johannes, 1810
1	MS 9292	Joe Schoeniger, 8321
1	MS 1411	Jim Voigt, 1816
1	MS 1082	John D. Williams, 1725
1	MS 1245	David P. Adams, 1245
1	MS 1349	Hongyou Fan, 1815
1	MS 1245	John Emerson, 2453

1 Prof. Cathy Clewett
Physics Department
Fort Hays State University
600 Park St.
Hays, KS 67601

1 Prof. Laurel Sillerud
Dept. of Biochemistry and Molecular Biology
University of New Mexico School of Medicine
Cancer Research and Treatment Center
Albuquerque, NM 87131

1 Dr. Andrew McDowell
New Mexico Resonance
2301 Yale Blvd SE, Suite C-1
Albuquerque, NM

1 Dr. Natalie Adolphi
New Mexico Resonance
2301 Yale Blvd SE, Suite C-1
Albuquerque, NM

2	MS 9018	Central Technical Files, 8944
2	MS 0899	Technical Library, 4536